S.T. Yau High School Science Award

RESEARCH REPORT

Name: Alyssa Yu
School: Poolesville High School
City/State: Poolesville, Maryland
Country: USA

Name of Supervising Teacher: Dr. Laura P. Schaposnik
Institution: University of Illinois Chicago
City/State: Chicago, Illinois
Country: USA

Title of Research Report: Spatiotemporal Super-Infection and Co-Infection Dynamics in Networks

Date: August 24, 2025

Note: Part of this report was recently released in an ArXiv preprint [1] co-authored by myself and my supervising teacher.

Spatiotemporal Super-Infection and Co-Infection Dynamics in Networks

Alyssa Yu

Abstract: Understanding interactions between the spread of multiple pathogens during an epidemic is crucial to assessing the severity of infections in living communities. We introduce two new Multiplex Bi-Virus Reaction-Diffusion models (MBRD) on multiplex metapopulation networks: the super-infection model (MBRD-SI) and the co-infection model (MBRD-CI). These models capture two-pathogen dynamics with spatial diffusion and cross-diffusion, allowing the prediction of infection clustering and large-scale spatial distributions. For a thorough investigation of the spatiotemporal evolution of two-pathogen epidemics, we first derive conditions for Turing and Turing-Hopf instability for pattern formation in both models. Then, through numerical experiments, we study the effects of pathogen virulence, superinfection and co-infection rates, and network topologies on epidemic hotspot formation and long-term prevalence. Our results highlight the role of multiplex structure in amplifying or suppressing co-circulating infections, and provide quantitative insight into conditions that drive persistent epidemic patterns. Beyond epidemiology, these findings have broader implications for multiplex contagion processes such as information diffusion and malware propagation.

Keywords: epidemic models, reaction-diffusion, Turing patterns, multiplex networks, super-infection, co-infection, bi-virus model, two-strain model

Contents

I. INTRODUCTION

Mathematical models for epidemiology have been crucial to understanding the spread of infections, from Ebola [2] to malaria [3]. During the COVID-19 pandemic, mathematical models informed policy decisions, including issued public health emergencies, lockdowns, and mask mandates worldwide [4]. To combat the 2024 measles outbreak in Chicago, Illinois, the Center for Disease Control used a compartmental dynamic model to predict new cases and inform an early response which included mass vaccinations [5].

The field of epidemiology originates from Hippocrates in ancient Greece [6], and has evolved significantly since. The first mathematical model for epidemiology was developed by Bernoulli [7] to study smallpox spread. Later, in 1927, Kermack and McKendrick introduced the compartmental SIR model [8], in which individuals are separated into the Susceptible, Infected, and Recovery populations.

Most epidemic models can be categorized as either stochastic or deterministic. There are a number of approaches to stochastic modeling, including Markov chains [9], cellular automata [10], stochastic differential equations [11], branching processes [12], and percolation [13]. While most deterministic models are compartmental, modifications can be made to structure them based on factors such as age [14] and risk [15]. Our study is based on the classic SIS model [16], in which individuals are compartmentalized into the Susceptible and Infected populations, and individuals become susceptible once again after recovery without lasting immunity.

There are a myriad of studies dedicated to understanding the spread of a single infectious disease. In this paper, we extend the typical SIS framework in the following two ways.

- We extend classic SIS models to two-pathogen models, formalized as the **Multiplex Bi-Virus Reaction-Diffusion framework (MBRD)**. Within this, we define the super-infection model **(MBRD-SI)** and the co-infection model **(MBRD-CI)**. While we refer to the infecting agents as "viruses" in this paper, these extensions can also capture the dynamics of interactions between viral strains while they spread across populations.

- Spatiotemporal epidemic modeling has emerged as a critical area in understanding infection spread. In many scenarios, the severity of infections in a region depends on infections in neighboring regions. As a result, factoring in spatial information leads to more accurate models. Moreover, spatial data and analysis are especially useful for identifying and targeting high-risk areas, particularly in the early stages of an epidemic [17]. Thus, we consider the spatial distribution of infections across a network of populations, which can represent towns, cities, or countries, depending on the spatial scale chosen. To do this, we integrate multiplex networks into our model so varying levels of movement between populations are accounted for.

The spread of infectious diseases can be characterized by diffusion processes [18, 19], and reaction-diffusion equations have been used to model the epidemic spread of a single pathogen [20, 21]. Reaction-diffusion dynamics can often simulate the clustering of infections that occurs between physical communities. For example, we observe that clustering occurs in both Figure 1 and Figure 2, showing that modeling with reaction-diffusion systems may explain some aspects of infection spread in the physical world. In this paper, reaction-diffusion mechanics allow us to describe the spatial distribution of infections in two-pathogen models by treating the susceptible state and each infected state as different morphogens.

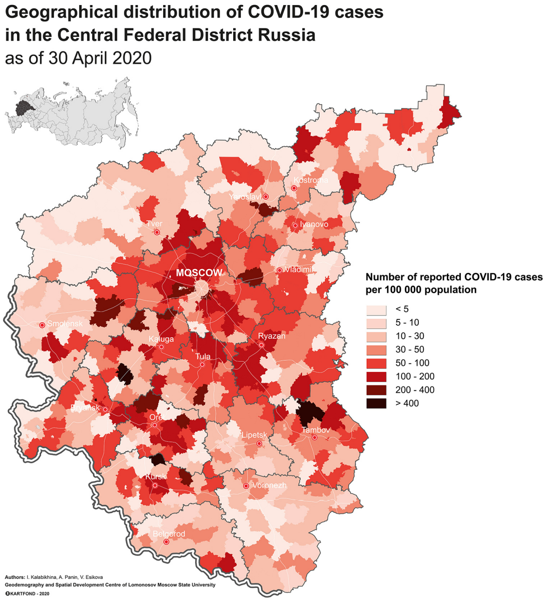

FIG. 1: Distribution of COVID-19 infections in the Central Federal District of Russia, from [22].

This paper makes both theoretical and simulation-based contributions to the study of two-pathogen dynamics. In the theoretical part of our paper, we make the following contributions:

- We establish two new ***Multiplex Bi-Virus Reaction-Diffusion models*** **(MBRD)** on multiplex networks: the super-infection model **(MBRD-SI)** and the co-infection model **(MBRD-CI)**. By incorporating reaction-diffusion and cross-diffusion dynamics, these models capture realistic spatial distributions of infections over large geographical ranges and account for complex network structures (see Section III).

- We perform instability analyses for reaction-diffusion systems with three (resp. four) morphogens on three-layer (resp. four-layer) multiplex networks. This includes explicit conditions for Turing and Turing-Hopf instabilities. To the

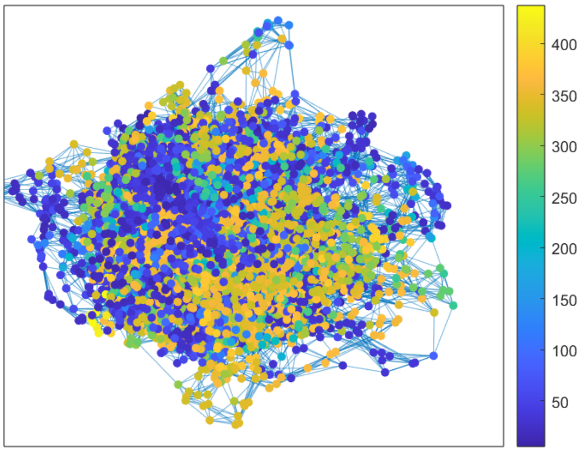

FIG. 2: Simulation of infection cases on a Watts-Strogatz network, created using the epidemic model from [20].

best of our knowledge, prior work has only addressed reaction-diffusion epidemic systems on two-layer multiplex networks (see Sections IV and V).

We also build on the MBRD framework to analyze bi-pathogen dynamics from a simulation-based standpoint, with an emphasis on the types of spatiotemporal phenomena that arise under different network and epidemiological conditions. We focus on two complementary perspectives:

- **Hotspot growth.** We investigate the formation and growth of stationary hotspots that emerge from perturbations to a steady state. Such hotspots, driven by Turing instability, can lead to system collapse. For example, cholera is largely endemic in countries such as Bangladesh, yet hotspots often occur due to seasonal plankton blooms [23]. While prior works such as [21] considered single-pathogen hotspots, no previous study has thoroughly examined this phenomenon in bi-pathogen dynamics through a simulation-based approach.

- **Point-source infections.** Infections often originate from localized events such as concerts, airports, or schools. Historical examples include Coxiella burnetii spreading from a dairy-goat farm in the Netherlands [24], or a campylobacteriosis outbreak from raw milk consumed on a school field trip [25]. In the context of bi-pathogen spread, we investigate point-source infections where both pathogens originate independently in the network, and analyze how MBRD-SI and MBRD-CI respond under varying parameter regimes.

Through our analysis of the different settings, we have several main results:

- Stationary hotspots can grow in severity over time under both MBRD-SI and MBRD-CI dynamics, potentially leading to system collapse. Varying network average degrees across the layers can inhibit pattern formation and growth.

- A higher superinfection coefficient accelerates the spread of the more severe pathogen, while a higher co-transmission coefficient accelerates the spread of co-infections. Moreover, lower removal rates of co-infected individuals can increase endemicity of co-infections.

- During the early stages of bi-pathogen spread, limiting migration of infected individuals is crucial to containment, verifying the importance of quarantine policies.

- Network topology strongly influences pathogen spread, offering a possible explanation for seasonal surges in outbreaks - even under bi-pathogen dynamics.

The remainder of this paper is organized as follows. Section II introduces preliminaries on Turing patterns. Section III introduces novel reaction-diffusion models MBRD-SI and MBRD-CI for super-infection and co-infection. Section IV establishes instability conditions for three-morphogen systems including the MBRD-SI model, while Section V treats the four-morphogen case including the MBRD-CI model. Section VI investigates how various factors influence pattern formation and hotspot growth. Section VII introduces metrics for analyzing spread from point sources and discusses the impact of model parameters and network layers. Section VIII connects our simulation results with real-world co-infection data. Finally, Section IX discusses potential applications that our framework can be used for. Finally, Section X concludes this paper with a summary of this work and future extensions.

II. BACKGROUND

In 1952, Turing proposed that reaction-diffusion dynamics trigger the formation of many patterns in nature (e.g., the pattern in Figure 3). These patterns, known as Turing patterns, are driven by interactions between substances, referred to as morphogens. Subsequently, Gierer and Meinhardt introduced the local autoactivation-lateral inhibition (LALI) framework in 1972, demonstrating that for Turing patterns to form, local self-activation and long-range inhibition must balance each other [26]. In 1990, Turing patterns were first confirmed experimentally in the chlorite-iodide-malonic acid (CIMA) reaction [27]. In the following, we first introduce Turing patterns on continuous domains and then Turing patterns on networks. We also discuss previous spatial epidemic models with either one or two pathogens.

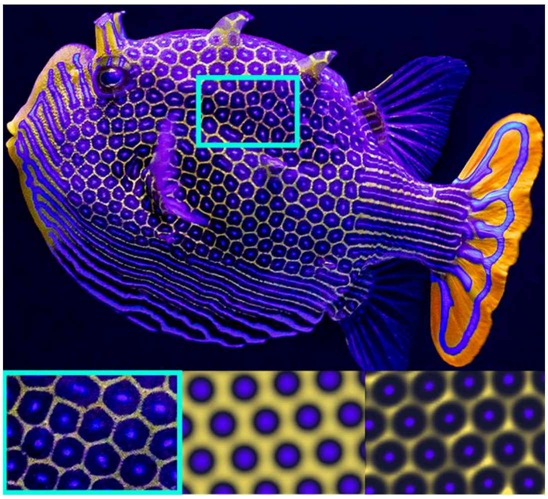

FIG. 3: A boxfish (top), a closeup of its pigmentation pattern (bottom-left), and simulations (bottom-center and right), from [28].

A. Turing Patterns on Continuous Domains

Turing patterns are formed by small fluctuations in the concentration of morphogens, which grow and settle into a spatially organized pattern. The instabilities relevant to this paper are Turing, Hopf, and Turing-Hopf instabilities, which are defined below.

Definition 1. *Turing instability* results in a stationary spatial pattern, *Hopf instability* results in temporal oscillations only, and *Turing-Hopf instability* results in both spatial and temporal oscillations over the same period of time.

For the most simple example, we consider two reaction-diffusion equations of the form,

$$\frac{\partial u}{\partial t} = f(u,v) + D_u \nabla^2 u, \tag{1}$$

$$\frac{\partial v}{\partial t} = g(u,v) + D_v \nabla^2 v, \tag{2}$$

where f and g describe the reaction kinetics of the morphogens, D_u and D_v are the diffusion coefficients and $\nabla^2 u = \partial^2 u/\partial x^2$ where x is the finite domain $[0, L]$. To obtain a unique pattern, we must also introduce a boundary condition. Most often, the boundary condition imposed is the *Neumann condition*, which specifies that there is no flux at the spatial boundary.

Theorem 1 (Turing instability conditions for Equations (1) and (2)). *[29, Equations (7.13), (7.16), (7.17)] Let $f_u := \partial f/\partial u$, $f_v := \partial f/\partial v$, $g_u := \partial g/\partial u$, and $g_v := \partial g/\partial v$. The conditions for Turing instability are*

$$\begin{aligned} f_u + g_v &< 0, \\ f_u g_v - f_v g_u &> 0, \\ D_v f_u + D_u g_v &> 2\sqrt{D_u D_v (f_u g_v - f_v g_u)}, \\ k_-^2 < \left(\frac{n\pi}{L}\right)^2 &< k_+^2, \end{aligned}$$

where

$$k_\pm^2 = \frac{f_u + g_v \pm \sqrt{(f_u+g_v)^2 - 4D_u D_v (f_u g_v - f_v g_u)}}{2 D_u D_v}.$$

Theorem 1 is proven by considering a small perturbation $(\hat{u}(x,t), \hat{v}(x,t))$ to the equilibrium state and linearizing the system with multivariable Taylor polynomial expansions. We then substitute an ansatz solution of the form $\hat{\boldsymbol{u}} = \boldsymbol{a} \exp(ikx + \lambda(k^2)t)$, where $\hat{\boldsymbol{u}} := \begin{pmatrix} \hat{u} & \hat{v} \end{pmatrix}^T$, $\boldsymbol{a}$ is a constant vector, k is the wave number or the number of spatial oscillations within a certain length, and λ is the temporal growth rate. From this, we obtain the characteristic equation $\lambda^2 - (f_u + g_v)\lambda + (f_u g_v - f_v g_u) = 0$, and with further analysis, we obtain the four conditions above. We will use a similar idea for the instability analysis in this paper.

B. Turing Patterns on Networks

Most Turing models proposed have been on continuous domains; however, the branch of Turing patterns on complex networks, first introduced in [30], has recently become prevalent.

In the following, we introduce Turing patterns on complex networks. Consider a unweighted network $G := (V, E)$ with $|V| = N$, where an edge from node i to node j is denoted by (i,j). We assume here that G is undirected. The entries of the adjacency matrix $\boldsymbol{A}(G)$ are defined as

$$A_{ij}^G := \begin{cases} 1, & \text{if } (i,j) \in E, \\ 0, & \text{otherwise} \end{cases}$$

We define a matrix $\boldsymbol{L}(G)$ as a function of graph G as follows:

Definition 2. If G is a graph with N nodes, then we define $\boldsymbol{L}(G)$ to be an $N \times N$ matrix with entries

$$L_{ij} := A_{ij}^G - \delta_{ij} k_i^G,$$

where

$$\delta_{ij} := \begin{cases} 1, & \text{if } i = j, \\ 0, & \text{otherwise.} \end{cases}$$

and A_{ij}^G are the entries of the adjacency matrix $\boldsymbol{A}(G)$. Moreover k_i^G is the degree of node i and satisfies $k_i^G := \sum_{j=1}^N A_{ij}^G$.

Note that our definition of $\boldsymbol{L}$ is the negative of the combinatorial Laplacian. The diffusion of a morphogen from node j to node i is of rate $D_u(u_j - u_i)$. We can add these rates to get the total amount of the morphogen that enters a node. Thus, the amount of substance entering node i is

$$\dot{u}_i = D_u \sum_{j=1}^{n} A_{ij}(u_j - u_i) = D_u \left(\sum_{j=1}^{n} A_{ij} u_j \right) - D_u k_i u_i$$
$$= D_u \sum_{j=1}^{n} L_{ij} u_j .$$

In a network, a two-morphogen reaction-diffusion system is formulated as

$$\frac{du_i}{dt} = f(u_i, v_i) + D_u \sum_{j=1}^{n} L_{ij} u_j ,$$
$$\frac{dv_i}{dt} = g(u_i, v_i) + D_v \sum_{j=1}^{n} L_{ij} v_j ,$$

for all $i = 1, 2, \ldots, n$, where L_{ij} are the entries of the combinatorial Laplacian.

C. Previous Epidemic Models

In reaction-diffusion epidemic models, the states, such as Susceptible and Infected, are treated as morphogens and the model is a function of the relative densities of those separate populations at every node. To the best of our knowledge, the first SI reaction-diffusion model was introduced by Webb [31] in 1981. This framework has been extended to analyze the spread of specific pathogens. For example, Bai *et al.* [32] proposed a malaria reaction-diffusion model, accounting for seasonality and incubation. Likewise, Wang *et al.* [33] studied a similar COVID model accounting for superspreaders and asymptomatic cases on a continuous domain. Recent research has also proposed epidemic models on complex networks. For instance, Duan *et al.* [20] investigated a SIS reaction-diffusion model on a single-layer complex network.

Epidemic models have been studied on two-layer multiplex networks, where layers have the same sets of nodes but can have different connectivity and house different diffusing morphogens representing different aspects of the system. Zhao and Shen introduced a reaction-diffusion epidemic model with S and I states on a two-layer network [21] with cross-diffusion, meaning that, when the movement of individuals on the S and I layers induce diffusion on the other layer. Reaction-diffusion two-strain models have also been proposed on continuous domains. Shi and Zhao [34] analyzed a reaction-diffusion two-strain malaria model and Lu *et al.* [35] introduced a two-strain COVID model.

To the extent of our knowledge, no previous reaction-diffusion models have considered **Multiplex Bi-Virus Reaction-Diffusion frameworks**, including the super-infection case (MBRD-SI) or the co-infection case (MBRD-CI), on discrete domains.

Parameters for Epidemic Models	
Symbol	**Description**
β_1	Transmission rate of pathogen 1 from population infected only with pathogen 1
β_2	Transmission rate of pathogen 2 from population infected only with pathogen 1
β_{10}	Transmission rate of pathogen 1 only from co-infected population
β_{02}	Transmission rate of pathogen 2 only from co-infected population
β_{12}	Transmission rate of co-infection from co-infected population
γ_1	Recovery rate for pathogen 1
γ_2	Recovery rate for pathogen 2
α_1	Virulence of pathogen 1
α_2	Virulence of pathogen 2
r	Natural growth of susceptible population
K	Maximum environmental capacity density
A	Critical spatial carrying capacity density
μ	Natural mortality rate
σ	Rate of host takeover by the more virulent strain
d_{11}	Diffusion rate of susceptible population
d_{12}	Cross-diffusion rate induced by movement of population infected with pathogen 1
d_{13}	Cross-diffusion rate induced by movement of population infected with pathogen 2
d_{22}	Diffusion rate of population infected with pathogen 1
d_{33}	Diffusion rate of population infected with pathogen 2

TABLE I: Parameters used in the epidemic models.

III. EPIDEMIC MODELS

In this section, we develop the two **Multiplex Bi-Virus Reaction-Diffusion models**: the superinfection model **(MBRD-SI)** and the co-infection model **(MBRD-CI)**. In this context, super-infection refers to when pathogens cannot coexist in the same host and a more virulent pathogen can “steal” the host from a less virulent pathogen. Co-infection describes scenarios when a host can be infected with both viruses at once. In our co-infection model, no pathogen can “steal” hosts from the other.

In addition to interactions between two different viruses, our superinfection and co-infection models apply to interactions between different strains of the same virus [36–38]. Following conventional notation, we use S, I_1, I_2, and I_{12} in the classic SIS model to represent the densities of the susceptible population, population mono-infected by pathogen 1, population mono-infected by pathogen 2, and the co-infected population. We will sometimes refer to a host infected by pathogen 1 (resp. pathogen 2) as I-infected (J-infected).

When discussing the reaction-diffusion equations, we use the symbols S, I, J, and C instead to represent the susceptible, I-infected (both mono and co-infections), J-

infected, and co-infected population densities. Note that Table I introduces the key notation used in Sections III A and III B.

A. The Super-Infection Model (MBRD-SI)

The following superinfection SIS model was developed by Nowak and May in 1994 [36]:

$$\begin{aligned}\frac{dS}{dt} &= B - (\mu + \beta_1 I_1 + \beta_2 I_2)S,\\ \frac{dI_1}{dt} &= I_1(\beta_1 S - \mu - \alpha_1 - \sigma\beta_2 I_2),\\ \frac{dI_2}{dt} &= I_2(\beta_2 S - \mu - \alpha_2 + \sigma\beta_2 I_1),\\ 1 &= S + I_1 + I_2,\end{aligned}$$

where S, I_1, and I_2 represent the proportion of the population that is susceptible, infected by the first strain, and infected by the second strain, respectively. It is assumed that both strains cannot coinfect a single host. Moreover, this model assumes that pathogen 2 is more virulent than pathogen 1. Note that σ represents the relative rate of superinfection of hosts already infected with pathogen 1 relative to the transmission of pathogen 2 to uninfected hosts. When $\sigma > 1$, hosts already infected with pathogen 1 are more likely than uninfected hosts to become infected with pathogen 2.

Inspired by [21], we incorporate a logistic growth framework to model the growth of the susceptible population, which is suited for reaction dynamics in small communities or cities. Due to factors such as low social capital, populations with low densities will grow relatively slowly. Moreover, due to resource shortages and lower quality of life, populations with high densities will often converge to a carrying capacity, exhibiting the Allee effect.

We adjust this model by adding in recovery rates from both pathogens and modify it so that S, I_1, and I_2 represent the number of individuals or the population densities, as shown in the following system:

$$\begin{aligned}\frac{dS}{dt} &= rS\left(1 - \frac{S}{K}\right)\left(\frac{S}{A} - 1\right) - \frac{(\beta_1 I_1 + \beta_2 I_2)S}{S + I_1 + I_2}\\ &\quad + \gamma_1 I_1 + \gamma_2 I_2 - \mu S,\\ \frac{dI_1}{dt} &= I_1\left(\frac{\beta_1 S}{S + I_1 + I_2} - \mu - \alpha_1 - \gamma_1 - \frac{\sigma\beta_2 I_2}{S + I_1 + I_2}\right),\\ \frac{dI_2}{dt} &= I_2\left(\frac{\beta_2 S}{S + I_1 + I_2} - \mu - \alpha_2 - \gamma_2 + \frac{\sigma\beta_2 I_1}{S + I_1 + I_2}\right).\end{aligned}$$

We represent this system with Figure 4. The susceptible population growth is described by $rS\left(1 - \frac{S}{K}\right)\left(\frac{S}{A} - 1\right)$. The movement from the susceptible population to the two infected populations are represented by $\frac{\beta_1 I_1 S}{S+I_1+I_2}$ and $\frac{\beta_2 I_2 S}{S+I_1+I_2}$. The movement from the I-infected to J-infected population due to superinfection is $\frac{\sigma\beta_2 I_1 I_2}{S+I_1+I_2}$. The movement from either infected population to the susceptible population due to recovery is represented by $\gamma_1 I$ and $\gamma_2 J$. Finally, the total population deaths are represented by μS, $(\mu + \alpha_1)I$, and $(\mu + \alpha_2)J$ for the three populations, respectively.

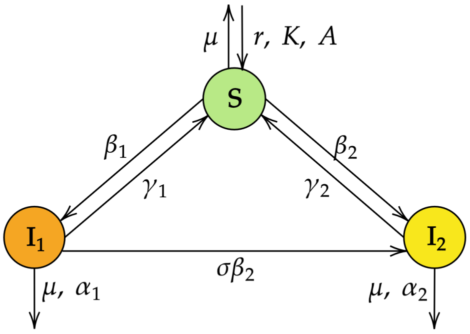

FIG. 4: Flowchart for the super-infection model (MBRD-SI).

We consider the three-layer multiplex network pictured in Figure 5, where each layer has the same set of nodes. In an epidemiological context, it is most reasonable for the average degree of the I and J layers to be the same or lower than the average degree of the S layer, as infected people tend to migrate less.

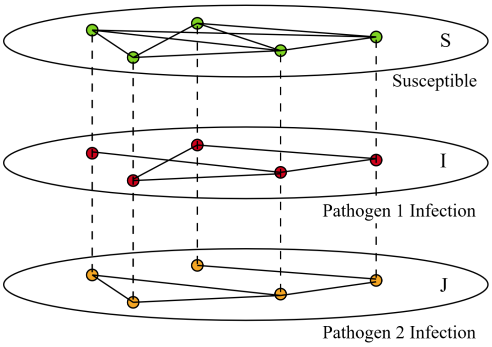

FIG. 5: Three-layer multiplex network for MBRD-SI.

In order to understand the spatial distribution of infected populations, we treat the S, I, and J population densities as morphogens which diffuse on the corresponding separate layers of Figure 5. We let S_i, I_i, and J_i be the densities of the susceptible population, I-infected population, and J-infected population, respectively. We denote the S, I, and J layers to be graphs G_S, G_I, and G_J, respectively. Then, we let $\boldsymbol{L}^{(S)} = \boldsymbol{L}(G_S)$, $\boldsymbol{L}^{(I)} = \boldsymbol{L}(G_I)$, and $\boldsymbol{L}^{(J)} = \boldsymbol{L}(G_J)$, defined according to Definition 2. We also denote the entries of $\boldsymbol{L}^{(S)}$, $\boldsymbol{L}^{(I)}$, and $\boldsymbol{L}^{(J)}$ in row i and column j to be $L_{ij}^{(S)}$, $L_{ij}^{(I)}$, and $L_{ij}^{(J)}$.

Then, we propose the following reaction-diffusion model:

$$\begin{aligned}\frac{dS_i}{dt} &= rS_i\left(1-\frac{S_i}{K}\right)\left(\frac{S_i}{A}-1\right)-\frac{(\beta_1 I_i+\beta_2 J_i)S_i}{S_i+I_i+J_i}\\ &\quad+\gamma_1 I_i+\gamma_2 J_i-\mu S\\ &\quad+d_{11}\sum_{j=1}^{N}L_{ij}^{(S)}S_j+d_{12}\sum_{j=1}^{N}L_{ij}^{(I)}I_j+d_{13}\sum_{j=1}^{N}L_{ij}^{(J)}J_j,\\ \frac{dI_i}{dt} &= I_i\left(\frac{\beta_1 S_i}{S_i+I_i+J_i}-\mu-\alpha_1-\gamma_1-\frac{\sigma\beta_2 J_i}{S_i+I_i+J_i}\right)\\ &\quad+d_{22}\sum_{j=1}^{N}L_{ij}^{(I)}I_j,\\ \frac{dJ_i}{dt} &= J_i\left(\frac{\beta_2 S_i}{S_i+I_i+J_i}-\mu-\alpha_2-\gamma_2+\frac{\sigma\beta_2 I_i}{S_i+I_i+J_i}\right)\\ &\quad+d_{33}\sum_{j=1}^{N}L_{ij}^{(J)}J_j.\end{aligned} \tag{3}$$

We include the cross-diffusion terms $d_{12}\sum_{j=1}^{N}L_{ij}^{(I)}I_j$ and $d_{13}\sum_{j=1}^{N}L_{ij}^{(J)}J_j$ to indicate how the susceptible population moves in response to infected population densities. In particular, when d_{12} is positive (resp. negative), susceptible individuals gravitate toward areas with a low (resp. high) density of individuals infected with pathogen 1, and when d_{13} is positive (resp. negative), susceptible individuals gravitate toward areas with a low (resp. high) density of individuals infected with pathogen 2.

B. The Co-Infection Models (MBRD-CI)

The co-infection SIS model proposed by Gao *et al.* in 2016 [39] is

$$\begin{aligned}\frac{dS}{dt} &= \mu-(\lambda_1+\lambda_2+\lambda_{12\to1}+\lambda_{12\to12}+\lambda_{12\to2})S\\ &\quad+(\gamma_1 I_1+\gamma_2 I_2)-\mu S,\\ \frac{dI_1}{dt} &= (\lambda_1+\lambda_{12\to1})S-(\lambda_2+\lambda_{12\to2}+\lambda_{12\to12})I_1\\ &\quad+(\gamma_2 I_{12}-\gamma_1 I_1)-\mu I_1,\end{aligned}$$

$$\begin{aligned}\frac{dI_2}{dt} &= (\lambda_2+\lambda_{12\to2})S-(\lambda_1+\lambda_{12\to1}+\lambda_{12\to12})I_2\\ &\quad+(\gamma_1 I_{12}-\gamma_2 I_2)-\mu I_2,\\ \frac{I_{12}}{dt} &= \lambda_{12\to12}S+(\lambda_2+\lambda_{12\to2}+\lambda_{12\to12})I_1\\ &\quad+(\lambda_1+\lambda_{12\to1}+\lambda_{12\to12})I_2-(\gamma_1+\gamma_2)I_{12}-\mu I_{12},\\ 1 &= S+I_1+I_2+I_{12},\end{aligned}$$

where $\lambda_1 := \beta_1 I_1$, $\lambda_2 := \beta_2 I_2$, $\lambda_{12\to12} := \beta_{12}I_{12}$, $\lambda_{12\to1} := \beta_{10}I_{12}$, and $\lambda_{12\to2} := \beta_{02}I_{12}$.

Note that the dynamics of the two pathogens can be described in the following four ways [39]:

- In non-interaction transmission, the presence of the two diseases do not affect each other. In the model, this translates to $\beta_{12}+\beta_{10}=\beta_1$ and $\beta_{12}+\beta_{02}=\beta_2$.
- Mutual enhancement occurs when $\beta_{12}+\beta_{10}>\beta_1$ and $\beta_{12}+\beta_{02}>\beta_2$.
- The enhancement of one pathogen and inhibition of the other occurs when either $\beta_{12}+\beta_{10}>\beta_1$ and $\beta_{12}+\beta_{02}<\beta_2$, or
$\beta_{12}+\beta_{10}<\beta_1$ and $\beta_{12}+\beta_{02}>\beta_2$.
- Mutual inhibition occurs when $\beta_{12}+\beta_{10}<\beta_1$ and $\beta_{12}+\beta_{02}<\beta_2$.

We define I (resp. J) to represent the total I-infected (resp. J-infected) density, including both mono- and co-infections, and use C in place of I_{12}. We combine mono- and co-infections because we assume that the two pathogens exhibit independent diffusion dynamics, and we want to consider the diffusion of the population densities associated with both mono- and co-infections. After making these modifications, we have

$$\begin{aligned}\frac{dS}{dt} &= B-(\beta_1 I+\beta_2 J)S\\ &\quad-(\beta_{10}+\beta_{02}+\beta_{12}-\beta_1-\beta_2)CS\\ &\quad+\gamma_1 I+\gamma_2 J-(\gamma_1+\gamma_2)C-\mu S,\\ \frac{dI}{dt} &= [\beta_1 I+(\beta_{10}+\beta_{12}-\beta_1)C](S+J-C)-\gamma_1 I\\ &\quad-\alpha_1(I-C)-\alpha_{12}C-\mu I,\\ \frac{dJ}{dt} &= [\beta_2 J+(\beta_{02}+\beta_{12}-\beta_2)C](S+I-C)-\gamma_2 J\\ &\quad-\alpha_2(J-C)-\alpha_{12}C-\mu J,\\ \frac{dC}{dt} &= \beta_{12}CS+[\beta_2 J+(\beta_{02}+\beta_{12}-\beta_2)C](I-C)\\ &\quad+[\beta_1 I+(\beta_{10}+\beta_{12}-\beta_1)C](J-C)\\ &\quad-(\gamma_1+\gamma_2+\alpha_{12})C-\mu C,\\ 1 &= S+I+J-C.\end{aligned}$$

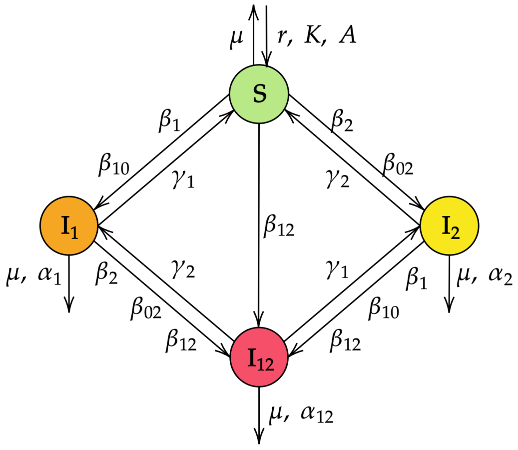

FIG. 6: Flowchart for the co-infection model (MBRD-CI).

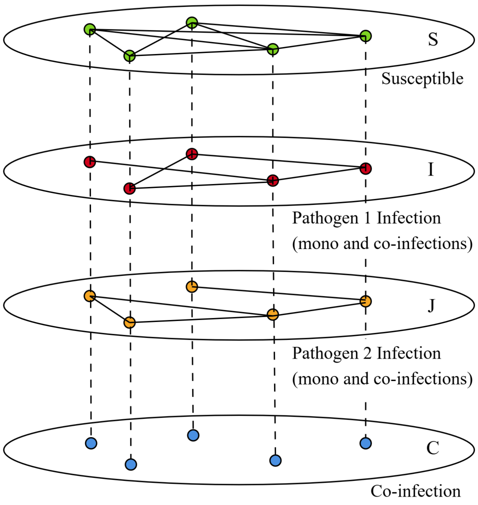

FIG. 7: Four-layer multiplex network for MBRD-CI.

We modify this model so that S, I, J, and C account for either the number of individuals or population densities. Moreover, we adopt a logistic growth framework instead of a constant birth rate, as follows:

$$
\begin{aligned}
\frac{dS}{dt} &= rS\left(1-\frac{S}{K}\right)\left(\frac{S}{A}-1\right) - \frac{(\beta_1 I+\beta_2 J)S}{S+I+J-C} \\
&\quad - \frac{(\beta_{10}+\beta_{02}+\beta_{12}-\beta_1-\beta_2)CS}{S+I+J-C} \\
&\quad + \gamma_1 I + \gamma_2 J - (\gamma_1+\gamma_2)C - \mu S, \\
\frac{dI}{dt} &= [\beta_1 I + (\beta_{10}+\beta_{12}-\beta_1)C]\cdot\frac{S+J-C}{S+I+J-C} - \gamma_1 I \\
&\quad - \alpha_1(I-C) - \alpha_{12}C - \mu I, \\
\frac{dJ}{dt} &= [\beta_2 J + (\beta_{02}+\beta_{12}-\beta_2)C]\cdot\frac{S+I-C}{S+I+J-C} - \gamma_2 J \\
&\quad - \alpha_2(J-C) - \alpha_{12}C - \mu J, \\
\frac{dC}{dt} &= \frac{\beta_{12}CS}{S+I+J-C} + \frac{[\beta_2 J + (\beta_{02}+\beta_{12}-\beta_2)C](I-C)}{S+I+J-C} \\
&\quad + \frac{[\beta_1 I + (\beta_{10}+\beta_{12}-\beta_1)C](J-C)}{S+I+J-C} \\
&\quad - (\gamma_1+\gamma_2+\alpha_{12})C - \mu C,
\end{aligned}
$$

Recall that our model has four states: S, I_1, I_2, and I_{12}, which are the susceptible, pathogen 1 mono-infected, pathogen 2 mono-infected, and co-infected densities. This system can be represented by Figure 6. The susceptible population has birth and natural death rates represented by $r\left(1-\frac{S}{K}\right)\left(\frac{S}{A}-1\right)$ and μS, respectively. The movement of individuals from S to the mono-infected states and from the mono-infected states to I_{12} are controlled by the infection rates. The movement of individuals from I_{12} back to a mono-infected state, as well as from a mono-infected state back to S, are controlled by the recovery rates. Finally, deaths in the I_1, I_2, and I_{12} populations include both natural and infection-related deaths.

We introduce the four-layer multiplex network in Figure 7. For the most part, we assume again that the average degrees of the I and J layers are less than the average degree of the S layer. Only the S, I, and J layers experience diffusion and thus, edges are not included in the C layer. This is because the relative density for each node on the C layer can directly be calculated from the densities of the corresponding nodes on the other three layers.

We treat the S, I, and J populations as morphogens and let S_i, I_i, J_i, and C_i be the densities of their corresponding populations on node i. Letting G_S, G_I, and G_J be the networks on layers S, I, and J, we establish the same definitions for $\boldsymbol{L}^{(S)}$, $\boldsymbol{L}^{(I)}$, and $\boldsymbol{L}^{(J)}$, and their respective entries $L_{ij}^{(S)}$, $L_{ij}^{(I)}$, and $L_{ij}^{(J)}$ as our superinfection model in Equation (3).

Then, we have

$$
\begin{aligned}
\frac{dS_i}{dt} &= rS_i\left(1-\frac{S_i}{K}\right)\left(\frac{S_i}{A}-1\right) - \frac{(\beta_1 I_i+\beta_2 J_i)S_i}{S_i+I_i+J_i-C_i} \\
&\quad - \frac{(\beta_{10}+\beta_{02}+\beta_{12}-\beta_1-\beta_2)C_iS_i}{S_i+I_i+J_i-C_i} \\
&\quad + \gamma_1 I_i + \gamma_2 J_i - (\gamma_1+\gamma_2)C_i - \mu S_i \\
&\quad + d_{11}\sum_{j=1}^{N} L_{ij}^{(S)} S_j + d_{12}\sum_{j=1}^{N} L_{ij}^{(I)} I_j + d_{13}\sum_{j=1}^{N} L_{ij}^{(J)} J_j, \\
\frac{dI_i}{dt} &= [\beta_1 I_i + (\beta_{10}+\beta_{12}-\beta_1)C_i]\cdot\frac{S_i+J_i-C_i}{S_i+I_i+J_i-C_i} \\
&\quad - \gamma_1 I_i - \alpha_1(I_i-C_i) - \alpha_{12}C_i - \mu I_i \\
&\quad + d_{22}\sum_{j=1}^{N} L_{ij}^{(I)} I_j, \\
\frac{dJ_i}{dt} &= [\beta_2 J_i + (\beta_{02}+\beta_{12}-\beta_2)C_i]\cdot\frac{S_i+I_i-C_i}{S_i+I_i+J_i-C_i} \\
&\quad - \gamma_2 J_i - \alpha_2(J_i-C_i) - \alpha_{12}C_i - \mu J_i \\
&\quad + d_{33}\sum_{j=1}^{N} L_{ij}^{(J)} J_j,
\end{aligned}
\tag{4}
$$

$$
\begin{aligned}
\frac{dC_i}{dt} = &\frac{\beta_{12}C_iS_i}{S_i+I_i+J_i-C_i} \\
&+ \frac{[\beta_2 J_i + (\beta_{02}+\beta_{12}-\beta_2)C_i](I_i-C_i)}{S_i+I_i+J_i-C_i} \\
&+ \frac{[\beta_1 I_i + (\beta_{10}+\beta_{12}-\beta_1)C_i](J_i-C_i)}{S_i+I_i+J_i-C_i} \\
&- (\gamma_1+\gamma_2+\alpha_{12})C_i - \mu C_i.
\end{aligned}
$$

IV. THREE-STATE INSTABILITY ANALYSIS

In this section, we perform an instability analysis for reaction-diffusion models with three morphogens on networks. In particular, we first derive general instability conditions for such models on a three-layer multiplex network. Then, we establish additional conditions for a special case where the layers of the multiplex network are identical. The conditions discussed in this section apply to the three-layer model in Equation (3).

A. Instability Analysis on a Three-Layer Multiplex Network

We now derive the conditions for Turing and Turing-Hopf instability in a reaction-diffusion system for three distinct morphogens on a three-layer multiplex network. We consider the following system with morphogens S, I, and J, where S_i, I_i, and J_i are the densities of the morphogens in each node of the network.

$$\begin{aligned}\frac{dS_i}{dt} &= f(S_i, I_i, J_i)\\ &\quad + d_{11}\sum_{j=1}^{n} L_{ij}^{(S)} S_j + d_{12}\sum_{j=1}^{n} L_{ij}^{(I)} I_j + d_{13}\sum_{j=1}^{n} L_{ij}^{(J)} J_j,\\ \frac{dI_i}{dt} &= g(S_i, I_i, J_i) + d_{22}\sum_{j=1}^{n} L_{ij}^{(I)} I_j,\\ \frac{dJ_i}{dt} &= h(S_i, I_i, J_i) + d_{33}\sum_{j=1}^{n} L_{ij}^{(J)} J_j.\end{aligned}$$

Let (S^*, I^*, J^*) be the steady state densities on all nodes. We define f_S to be $\frac{\partial f}{\partial S}|_{(S^*,I^*,J^*)}$ and f_I, f_J, g_S, g_I, g_J, h_S, h_I, and h_J similarly. We introduce a perturbation $(\delta S_i, \delta I_i, \delta J_i)$ to the equilibrium densities. Then, by multinomial Taylor expansions, we have

$$\begin{aligned}\frac{d\delta S_i}{dt} &= f_S\delta S_i + f_I\delta I_i + f_J\delta J_i + d_{11}\sum_{j=1}^{n} L_{ij}^{(S)}\delta S_j\\ &\quad + d_{12}\sum_{j=1}^{n} L_{ij}^{(I)}\delta I_j + d_{13}\sum_{j=1}^{n} L_{ij}^{(J)}\delta J_j,\\ \frac{d\delta I_i}{dt} &= g_S\delta S_i + g_I\delta I_i + g_J\delta J_i + d_{22}\sum_{j=1}^{n} L_{ij}^{(I)}\delta I_j\\ \frac{d\delta J_i}{dt} &= h_S\delta S_i + h_I\delta I_i + h_J\delta J_i + d_{33}\sum_{j=1}^{n} L_{ij}^{(J)}\delta J_j.\end{aligned} \tag{5}$$

We approximate this system as follows:

$$\begin{aligned}\frac{d\delta S_i}{dt} &= f_S\delta S_i + f_I\delta I_i + f_J\delta J_i\\ &\quad - d_{11}k_i^{(S)}\delta S_i - d_{12}k_i^{(I)}\delta I_i - d_{13}k_i^{(J)}\delta J_i,\\ \frac{d\delta I_i}{dt} &= g_S\delta S_i + g_I\delta I_i + g_J\delta J_i - d_{22}k_i^{(I)}\delta I_i\\ \frac{d\delta J_i}{dt} &= h_S\delta S_i + h_I\delta I_i + h_J\delta J_i - d_{33}k_i^{(J)}\delta J_i.\end{aligned} \tag{6}$$

Letting $\boldsymbol{x}_i := (\delta S_i, \delta I_i, \delta J_i)^T$, we rewrite the system in Equation (6) as

$$\frac{d\boldsymbol{x}_i}{dt} = \begin{pmatrix} f_S - d_{11}k_i^{(S)} & f_I - d_{12}k_i^{(I)} & f_J - d_{13}k_i^{(J)}\\ g_S & g_I - d_{22}k_i^{(I)} & g_J\\ h_S & h_I & h_J - d_{33}k_i^{(J)}\end{pmatrix}\boldsymbol{x}_i \tag{7}$$

Let $\boldsymbol{M}$ be the matrix

$$\begin{pmatrix} f_S - d_{11}k_i^{(S)} - \lambda & f_I - d_{12}k_i^{(I)} & f_J - d_{13}k_i^{(J)}\\ g_S & g_I - d_{22}k_i^{(I)} - \lambda & g_J\\ h_S & h_I & h_J - d_{33}k_i^{(J)} - \lambda\end{pmatrix}.$$

We let $\boldsymbol{x}_i$ be of the form $\boldsymbol{a}\exp(ikx + \lambda t)$, where λ is the growth rate. Substituting this ansatz into Equation (7), the growth rate satisfies $\det(\boldsymbol{M}) = 0$.

We define

$$\begin{aligned} q_{11} &:= g_I h_J - g_J h_I, & q_{22} &:= h_J f_S - h_S f_J,\\ q_{33} &:= f_S g_I - f_I g_S, & q_{12} &:= h_S g_J - g_S h_J,\\ q_{13} &:= g_S h_I - g_I h_S, & m_{11} &:= d_{11}k_i^{(S)},\\ m_{22} &:= d_{22}k_i^{(I)}, & m_{33} &:= d_{33}k_i^{(J)},\\ m_{12} &:= d_{12}k_i^{(I)}, & m_{13} &:= d_{13}k_i^{(J)}.\end{aligned}$$

We also denote e_i to be the i-th elementary symmetric polynomial and

$$\begin{aligned} p_1 &:= f_S + g_I + h_J,\\ p_2 &:= q_{11} + q_{22} + q_{33},\\ p_3 &:= (f_S g_I h_J + f_I g_J h_S + f_J g_S h_I)\\ &\quad - (f_S g_J h_I + f_I g_S h_J + f_J g_I h_S).\end{aligned}$$

Finally, we define

$$A(x_1, x_2, x_3, x_4, x_5) := x_1 f_S + x_2 g_I + x_3 h_J + x_4 g_S + x_5 h_S,$$

and

$$B(x_1, x_2, x_3, x_4, x_5) := x_1 q_{11} + x_2 q_{22} + x_3 q_{33} + x_4 q_{12} + x_5 q_{13}.$$

Then we let

$$p(\lambda) := -\det(M) = \lambda^3 - b\lambda^2 + c\lambda - d = 0, \tag{8}$$

where

$$\begin{aligned} b &:= p_1 - e_1(m_{11}, m_{22}, m_{33})\\ c &:= p_2 + e_2(m_{11}, m_{22}, m_{33}) - p_1 e_1(m_{11}, m_{22}, m_{33})\\ &\quad + A(m_{11}, m_{22}, m_{33}, m_{12}, m_{13})\\ d &:= p_3 - B(m_{11}, m_{22}, m_{33}, m_{12}, m_{13}) - e_3(m_{11}, m_{22}, m_{33})\\ &\quad + A(m_{22}m_{33}, m_{33}m_{11}, m_{11}m_{22}, -m_{12}m_{33}, -m_{13}m_{22}).\end{aligned} \tag{9}$$

We denote the solutions to the system in Equation (9) to be λ_1, λ_2, and λ_3, where $\Re(\lambda_1) \geq \Re(\lambda_2) \geq \Re(\lambda_3)$. We prove the following two sets of necessary instability conditions:

Proposition 1 (Boundary conditions)**.** *We must have*

$$\begin{aligned} p_1 &< 0, & p_2 &> 0, \\ p_3 &< 0, & p_1p_2 &< p_3. \end{aligned}$$

Proof. Recall the previously stated definitions of p_1, p_2, and p_3. At equilibrium, there is no spatial diffusion, and the characteristic polynomial $p(\lambda)$ is

$$\lambda^3 - p_1\lambda^2 + p_2\lambda - p_3.$$

All roots have negative real parts because no perturbations can grow into oscillations. By Vieta's formulas, we have

$$\begin{aligned} p_1 &= \lambda_1 + \lambda_2 + \lambda_3 < 0, \\ p_2 &= \lambda_1\lambda_2 + \lambda_2\lambda_3 + \lambda_3\lambda_1 > 0, \\ p_3 &= \lambda_1\lambda_2\lambda_3 < 0. \end{aligned}$$

Moreover, $p_1p_2 < p_3$ follows from the Routh-Hurwitz criterion. □

The following definition differentiates between Turing and Turing-Hopf instability for systems of three interacting morphogens in this context. A similar definition for continuous domains is also stated in [40].

Definition 3. Turing instability occurs when every eigenvalue of M with a positive real part is real for every Laplacian eigenvalue k. Turing-Hopf instability occurs when some eigenvalues with a positive real part are not real at some Laplacian eigenvalue k.

This leads us to the following set of instability conditions:

Proposition 2 (Instability conditions I)**.** *We denote Δ_3 to be the cubic discriminant $18bcd - 4b^3d + b^2c^2 - 4c^3 - 27d^2$. For Turing instability to occur, we have $c < 0$ must be true under the condition that $\Delta_3 = 18bcd - 4b^3d + b^2c^2 - 4c^3 - 27d^2 > 0$ and both $c > 0$ and $d > 0$ must both be true under the condition that $\Delta_3 < 0$. For Turing-Hopf instability to occur, we must have $\Delta_3 < 0$ and $d < 0$.*

Proof. Recall the definitions from Equations (8) and (9). Either all roots of $p(\lambda)$ are real or there is one real root and two complex roots.

If the discriminant $\Delta_3 = 18bcd - 4b^3d + b^2c^2 - 4c^3 - 27d^2$ is greater than 0, we have three distinct real roots, which we call x_1, y_1, and z_1. We assume without loss of generality that $x_1 > y_1 > z_1$. For any spatial instability to occur, there must be an nonzero number of positive roots because a perturbation must grow into an oscillation. Recall that $b = p_1 - e_1(m_{11}, m_{22}, m_{33})$ and m_{11}, m_{22}, and m_{33} are positive by definition. Then, because $p_1 < 0$ by Proposition 1, we have $b < 0$, we have that $p(\lambda)$ must have least one negative root and $x_1 < -(y_1 + z_1)$. First, if $x_1 > 0$ and $0 > y_1 > z_1$, it follows that $c = z_1(x_1 + y_1) + x_1y_1 < x_1y_1 - (x_1 + y_1)^2 < 0$ and $d = x_1y_1z_1 > 0$. Second, if $x_1 > y_1 > 0$ and $z_1 < 0$, then $c = x_1(y_1 + z_1) + y_1z_1 < y_1z_1 - (y_1 + z_1)^2 < 0$ and $d = x_1y_1z_1 < 0$. Thus, $c < 0$ must be true if $\Delta > 0$, assuming that spatial oscillations occur.

If the discriminant $\Delta = 18bcd - 4b^3d + b^2c^2 - 4c^3 - 27d^2$ is less than 0, there exist nonreal roots. Let these roots be $x_2 + y_2i$, $x_2 - y_2i$, and z_2, where x_2 and y_2 are positive, and z_2 are real numbers. By Vieta's formulas, we have $b = 2x_2 + z_2$, $c = x_2^2 + y_2^2 + 2x_2z_2$, and $d = z_2(x_2^2 + y_2^2)$. Recall that b is always negative. For spatial oscillations (Turing or Turing-Hopf) to occur, at least one root must have a positive real part. Thus either $x_2 > 0$ and $z_2 < 0$, or $x_2 < 0$ and $z_2 > 0$. First, if $z_2 < -\frac{x_2^2+y_2^2}{2x_2}$, we have $c < 0$ and $d < 0$. Second, when $-\frac{x_2^2+y_2^2}{2x_2} < z_2 < 0$, we have $c > 0$ and $d < 0$. Third, when $z_2 > 0$, we have $c > 0$ and $d > 0$.

It directly follows from Definition 3 that Turing instability can only occur when all roots are real or there are two complex roots with negative real parts. Turing-Hopf instability occurs when two roots are complex with positive real parts. The theorem statement thus directly follows from this definition and the analysis above. □

B. Instability Analysis on a Single-Layer Network

We shall derive additional instability conditions for the special case of Subsection IV A where all layers are identical, which collapses to a single layer network.

We denote G_A to be the single layer network, and $\boldsymbol{L_A} = \boldsymbol{L}(G_A)$ as defined in Definition 2. Inspired by [41], we express the perturbations $(\delta S_i, \delta I_i, \delta J_i)$ as

$$\left(\sum_{v=1}^{N} c_v^1 e^{\lambda_v t} \phi_i^{(v)}, \sum_{v=1}^{N} c_v^2 e^{\lambda_v t} \phi_i^{(v)}, \sum_{v=1}^{N} c_v^3 e^{\lambda_v t} \phi_i^{(v)} \right),$$

where μ_v is the v-th eigenvalue of $\boldsymbol{L}_A$ with corresponding eigenvector $\phi_v = \left(\phi_1^{(v)}, \dots, \phi_N^{(v)}\right)^T$, and λ_v is the growth rate of the v-th spatial mode.

We let

$$\boldsymbol{N} := \begin{pmatrix} f_S + d_{11}\mu_v & f_I + d_{12}\mu_v & f_J + d_{13}\mu_v \\ g_S & g_I + d_{22}\mu_v & g_J \\ h_S & h_I & h_J + d_{33}\mu_v \end{pmatrix}. \quad (10)$$

When we substitute the ansatzes in Equation (10) into the system in Equation (5), we have

$$\lambda_v \boldsymbol{y}_v = \boldsymbol{N}\boldsymbol{y}_v,$$

where $\boldsymbol{y}_v := \begin{pmatrix} c_v^1 & c_v^2 & c_v^3 \end{pmatrix}^T$.

We let $\boldsymbol{N}$ be the matrix

$$\begin{pmatrix} f_S + d_{11}\mu_v & f_I + d_{12}\mu_v & f_J + d_{13}\mu_v \\ g_S & g_I + d_{22}\mu_v & g_J \\ h_S & h_I & h_J + d_{33}\mu_v \end{pmatrix}.$$

Thus, the eigenvalue μ_v of $\boldsymbol{L}_A$ and eigenvalue λ_v of $\boldsymbol{N}$ for node v satisfy

$$\det(\boldsymbol{N}) = 0.$$

The characteristic polynomial is

$$\lambda_v^3 - b_1(\mu_v)\lambda_v^2 + c_1(\mu_v)\lambda_v - d_1(\mu_v) = 0, \tag{11}$$

where

$$\begin{aligned}
b_1(\mu_v) &\coloneqq p_1 + e_1(d_{11}, d_{22}, d_{33})\mu_v, \\
c_1(\mu_v) &\coloneqq p_2 \\
&\quad + \left[p_1 e_1(d_{11}, d_{22}, d_{33}) - A(d_{11}, d_{22}, d_{33}, d_{12}, d_{13})\right]\mu_v \\
&\quad + e_2(d_{11}, d_{22}, d_{33})\mu_v^2, \\
d_1(\mu_v) &\coloneqq p_3 + B(d_{11}, d_{22}, d_{33}, d_{12}, d_{13})\mu_v \\
&\quad + A(d_{11}d_{22}, d_{22}d_{33}, d_{33}d_{11}, -d_{12}d_{33}, -d_{13}d_{22})\mu_v^2 \\
&\quad + e_3(d_{11}, d_{22}, d_{33})\mu_v^3.
\end{aligned} \tag{12}$$

For simplicity, let

$$\begin{aligned}
A_1 &\coloneqq A(d_{11}, d_{22}, d_{33}, d_{12}, d_{13}), \\
A_2 &\coloneqq A(d_{22}d_{33}, d_{33}d_{11}, d_{11}d_{22}, -d_{12}d_{33}, -d_{13}d_{22}), \\
B_1 &\coloneqq B(d_{11}, d_{22}, d_{33}, d_{12}, d_{13}).
\end{aligned} \tag{13}$$

Then, we denote

$$\begin{aligned}
b_0 &\coloneqq p_2, & b_1 &\coloneqq A_1 - p_1 e_1(d_{11}, d_{22}, d_{33}), \\
b_2 &\coloneqq e_2(d_{11}, d_{22}, d_{33}), & \tilde{a}_0 &\coloneqq p_3, \\
\tilde{a}_1 &\coloneqq -B_1, & \tilde{a}_2 &\coloneqq A_2, \\
\tilde{a}_3 &\coloneqq -e_3(d_{11}, d_{22}, d_{33}).
\end{aligned} \tag{14}$$

Finally, note that $c_2(\phi_v)c_1(\phi_v) - c_0(\phi_v) = a_3\phi_v^3 + a_2\phi_v^2 + a_1\phi_v + a_0$, where

$$\begin{aligned}
a_0 &\coloneqq p_1 p_2 - p_3 \\
a_1 &\coloneqq p_1 A_1 + B_1 - p_2 e_1(d_{11}, d_{22}, d_{33}) - p_1^2 e_1(d_{11}, d_{22}, d_{33}) \\
a_2 &\coloneqq p_1 e_2(d_{11}, d_{22}, d_{33}) + p_1 e_1^2(d_{11}, d_{22}, d_{33}) \\
&\quad - e_1(d_{11}, d_{22}, d_{33})A_1 - A_2 \\
a_3 &\coloneqq e_3(d_{11}, d_{22}, d_{33}) \\
&\quad - e_1(d_{11}, d_{22}, d_{33})e_2(d_{11}, d_{22}, d_{33}).
\end{aligned} \tag{15}$$

In this scenario, Propositions 1 and 2 still hold. We prove the following proposition, which holds specifically for the case where the multiplex network layers are identical.

Proposition 3 (Instability conditions II). *Consider the following sets of inequalities:*

$$\begin{aligned}
&0 < a_2^2 - 3a_1a_3, \\
&0 < a_2 + \sqrt{a_2^2 - 3a_1a_3}, \\
&0 < 2a_2^3 + 2(a_2^2 - 3a_1a_3)^{3/2} - 9a_1a_2a_3 + 27a_0a_3^2,
\end{aligned} \tag{16}$$

and

$$\begin{aligned}
b_1 &< -\sqrt{4b_2b_0}, \\
3a_3\left(b_1 + \sqrt{b_1^2 - 4b_2b_0}\right) &\leq 2b_0\left(a_2 + \sqrt{a_2^2 - 3a_1a_3}\right), \\
2b_0\left(a_2 + \sqrt{a_2^2 - 3a_1a_3}\right) &\leq 3a_3\left(b_1 - \sqrt{b_1^2 - 4b_2b_0}\right), \\
g\left(\frac{-b_1 - \sqrt{b_1^2 - 4b_2b_0}}{2b_2}\right) &\leq 0, \\
g\left(\frac{-b_1 + \sqrt{b_1^2 - 4b_2b_0}}{2b_2}\right) &\leq 0,
\end{aligned} \tag{17}$$

where $g(y) \coloneqq b_2y^2 + b_1y + b_0$.

A Turing-Hopf instability in the system defined above occurs if and only if all inequalities in the system represented by Equation (16) are satisfied and at least one inequality in the system represented by Equation (17) is not satisfied. A Turing instability occurs if and only if a Turing-Hopf instability does not occur and all inequalities in the system represented by Equation (16) are satisfied.

Proof. Recall the definitions in Equations (11), (12), (13), (14), and (15). Let $\phi_v \coloneqq -\mu_v$ for every v. Then the characteristic polynomial is equivalent to $\lambda_v^3 - c_2(\phi_v)\lambda_v^2 + c_1(\phi_v)\lambda_v - c_0(\phi_v) = 0$, where

$$\begin{aligned}
c_2(\phi_v) &\coloneqq -e_1(d_{11}, d_{22}, d_{33})\phi_v + p_1, \\
c_1(\phi_v) &= b_2\phi_v^2 + b_1\phi_v + b_0, \\
c_0(\phi_v) &= \tilde{a}_3\phi_v^3 + \tilde{a}_2\phi_v^2 + \tilde{a}_1\phi_v + \tilde{a}_0.
\end{aligned}$$

It is well known that the eigenvalues μ_v are all nonpositive and $0 \in \{\mu_1, \ldots, \mu_N\}$. Thus ϕ_v is interchangable with k^2 in [40]. Verifying that the other assumptions used in [40] on the coefficients of $c_2(\phi_v)$, $c_1(\phi_v)$, and $c_0(\phi_v)$ are all true for our definitions above, we conclude that Proposition 3 follows from Theorem 1 in [40]. □

V. FOUR-STATE INSTABILITY ANALYSIS

We now derive the conditions for Turing and Turing-Hopf instability in a reaction-diffusion system for four distinct morphogens on a four-layer multiplex network, with diffusion occurring on only three layers. We consider the following system with morphogens S, I, J, and C, where S_i, I_i, J_i, and C_i are the densities of the morphogens in each node of the network. Because we consider diffusion on only the first three layers, the conditions discussed below apply to the MBRD-CI model in Equation (4).

$$\begin{aligned}\frac{dS_i}{dt} &= f(S_i, I_i, J_i, C_i)\\ &\quad + d_{11}\sum_{j=1}^{n} L_{ij}^{(S)} S_j + d_{12}\sum_{j=1}^{n} L_{ij}^{(I)} I_j + d_{13}\sum_{j=1}^{n} L_{ij}^{(J)} J_j,\\ \frac{dI_i}{dt} &= g(S_i, I_i, J_i, C_i) + d_{22}\sum_{j=1}^{n} L_{ij}^{(I)} I_j,\\ \frac{dJ_i}{dt} &= h(S_i, I_i, J_i, C_i) + d_{33}\sum_{j=1}^{n} L_{ij}^{(J)} J_j,\\ \frac{dC_i}{dt} &= l(S_i, I_i, J_i, C_i)..\end{aligned}$$

Let (S^*, I^*, J^*, C^*) be the steady state densities on all nodes. We define f_S to be $\frac{\partial f}{\partial S}|_{(S^*,I^*,J^*,C^*)}$ and f_I, f_J, f_C, g_S, g_I, g_J, g_C, h_S, h_I, h_J, h_C, l_S, l_I, l_J, and l_C similarly. We introduce a perturbation $(\delta S_i, \delta I_i, \delta J_i)$ to the equilibrium densities. Then, by multinomial Taylor expansions, we have

$$\begin{aligned}\frac{d\delta S_i}{dt} &= f_S\delta S_i + f_I\delta I_i + f_J\delta J_i + f_C\delta C_i + d_{11}\sum_{j=1}^{n} L_{ij}^{(S)}\delta S_j\\ &\quad + d_{12}\sum_{j=1}^{n} L_{ij}^{(I)}\delta I_j + d_{13}\sum_{j=1}^{n} L_{ij}^{(J)}\delta J_j,\\ \frac{d\delta I_i}{dt} &= g_S\delta S_i + g_I\delta I_i + g_J\delta J_i + g_C\delta C_i + d_{22}\sum_{j=1}^{n} L_{ij}^{(I)}\delta I_j\\ \frac{d\delta J_i}{dt} &= h_S\delta S_i + h_I\delta I_i + h_J\delta J_i + h_C\delta C_i + d_{33}\sum_{j=1}^{n} L_{ij}^{(J)}\delta J_j,\\ \frac{\delta C_i}{dt} &= l_S\delta S_i + l_I\delta I_i + l_J\delta J_i + l_C\delta C_i.\end{aligned} \tag{18}$$

We approximate this system as follows:

$$\begin{aligned}\frac{d\delta S_i}{dt} &= f_S\delta S_i + f_I\delta I_i + f_J\delta J_i + f_C\delta C_i\\ &\quad - d_{11}k_i^{(S)}\delta S_i - d_{12}k_i^{(I)}\delta I_i - d_{13}k_i^{(J)}\delta J_i,\\ \frac{d\delta I_i}{dt} &= g_S\delta S_i + g_I\delta I_i + g_J\delta J_i + g_C\delta C_i - d_{22}k_i^{(I)}\delta I_i\\ \frac{d\delta J_i}{dt} &= h_S\delta S_i + h_I\delta I_i + h_J\delta J_i + h_C\delta C_i - d_{33}k_i^{(J)}\delta J_i,\\ \frac{d\delta C_i}{dt} &= l_S\delta S_i + l_I\delta I_i + l_J\delta J_i + l_C\delta C_i.\end{aligned} \tag{19}$$

Letting $\boldsymbol{w}_i := (\delta S_i, \delta I_i, \delta J_i, \delta C_i)^T$, we rewrite the system in Equation (19) as

$$\frac{d\boldsymbol{w}_i}{dt} = \begin{pmatrix} f_S - d_{11}k_i^{(S)} & f_I - d_{12}k_i^{(I)} & f_J - d_{13}k_i^{(J)} & f_C\\ g_S & g_I - d_{22}k_i^{(I)} & g_J & g_C\\ h_S & h_I & h_J - d_{33}k_i^{(J)} & h_C\\ l_S & l_I & l_J & l_C \end{pmatrix}\boldsymbol{w}_i. \tag{20}$$

Recall the definitions of m_{11}, m_{22}, m_{33}, m_{12}, and m_{13} from the previous section. Let $\boldsymbol{P}$ be the matrix

$$\begin{pmatrix} f_S - m_{11} - \lambda & f_I - m_{12} & f_J - m_{13} & f_C\\ g_S & g_I - m_{22} - \lambda & g_J & g_C\\ h_S & h_I & h_J - m_{33} - \lambda & h_C\\ l_S & l_I & l_J & l_C - \lambda \end{pmatrix}.$$

We let $\boldsymbol{w}_i$ be of the form $\boldsymbol{a}\exp(ikx + \lambda t)$, where λ is the growth rate. Substituting this ansatz into Equation (7), the growth rate satisfies $\det(\boldsymbol{P}) = 0$.

We define

$$\begin{aligned} u_1 &:= m_{11}(l_I g_C h_J - l_I g_J h_C + l_J g_I h_C - l_J g_C h_I)\\ &\quad + m_{22}(l_S f_C h_J - l_S f_J h_C + l_J f_S h_C - l_J f_C h_S)\\ &\quad + m_{33}(l_S g_I f_C - l_S f_I g_C + l_I g_C h_J - l_I g_J h_C)\\ &\quad + m_{12}(l_S g_J h_C - l_S g_C h_J + l_J h_S g_C - l_J g_S h_C)\\ &\quad + m_{13}(l_S h_I g_C - l_S g_I h_C + l_I h_C g_S - l_I g_C h_S),\\ u_2 &:= l_S f_C m_{22} m_{33} + l_I g_C m_{11} m_{33} + l_J h_C m_{11} m_{22},\\ u_3 &:= l_S(f_I g_C - g_I f_C + f_J h_C - f_C h_J)\\ &\quad + l_I(g_J h_C - g_C h_J + g_S h_C - g_C h_S)\\ &\quad + l_J(g_C h_I - g_I h_C + f_C h_S - f_S h_C),\\ u_4 &:= m_{11}(l_I g_C + l_J h_C) + m_{22}(l_S f_C + l_J h_C)\\ &\quad + m_{33}(l_S f_C + l_I g_C) - l_S(g_C m_{12} + h_C m_{13}),\\ u_5 &:= l_S f_C + l_I g_C + l_J h_C. \end{aligned}$$

Recall the definitions of e_i, p_1, p_2, and p_3 from the previous section. We denote

$$\begin{aligned} r_1 &:= l_c - p_1,\\ r_2 &:= u_5 + l_c p_1 - p_2,\\ r_3 &:= u_3 + u_4 + l_C p_2 - p_3,\\ r_4 &:= \det\begin{pmatrix} f_S & f_I & f_J & f_C\\ g_S & g_I & g_J & g_C\\ h_S & h_I & h_J & h_C\\ l_S & l_I & l_J & l_C \end{pmatrix}. \end{aligned}$$

Recall the definitions of functions b, c, and d from the previous section. Then we let

$$r(\lambda) := \det(\boldsymbol{P}) = \lambda^4 - a'\lambda^3 + b'\lambda^2 - c'\lambda + d' = 0, \tag{21}$$

where

$$\begin{aligned} a' &:= l_C - b,\\ b' &:= u_5 + l_C b - c,\\ c' &:= u_3 + u_4 + l_C c - d,\\ d' &:= p_4 + u_1 - u_2 + l_C d. \end{aligned} \tag{22}$$

We denote the solutions to the system in Equation (22) to be λ_1, λ_2, and λ_3, where $\Re(\lambda_1) \geq \Re(\lambda_2) \geq \Re(\lambda_3)$. We prove the following two sets of necessary instability conditions:

Proposition 4 (Boundary conditions)**.** *For instability* *to occur, we must have*

$$\begin{aligned} r_4 &> 0, & r_3 &< 0, \\ r_2 &> 0, & r_1 &< 0, \\ r_1 r_4 &> r_2 r_3, & r_1 r_2 r_3 &> r_3^2 + r_1^2 r_4. \end{aligned}$$

Proof. Recall the previously stated definitions of r_1, p_2, r_3, and r_4. At equilibrium, there is no spatial diffusion, and the characteristic polynomial $r(\lambda)$ is

$$\lambda^4 - r_1\lambda^3 + r_2\lambda^2 - r_3\lambda + r_4.$$

All roots have negative real parts because no perturbations can grow into oscillations. By Vieta's formulas, we have

$$\begin{aligned} p_1 &= \lambda_1 + \lambda_2 + \lambda_3 + \lambda_4 < 0, \\ p_2 &= \sum_{cyc} \lambda_1\lambda_2 > 0, \\ p_3 &= \sum_{cyc} \lambda_1\lambda_2\lambda_3 < 0, \\ p_4 &= \lambda_1\lambda_2\lambda_3\lambda_4 > 0. \end{aligned}$$

Moreover, the conditions $r_1 r_4 > r_2 r_3$ and $r_1 r_2 r_3 > r_3^2 + r_1^2 r_4$ follow from the Routh-Hurwitz criterion. ☐

Proposition 5 (Instability conditions)**.** *Let Δ_4 be the quartic discriminant of $r(\lambda)$. If $\Delta_4 > 0$, then $4\lambda^3 - 3a'\lambda^2 + 2b'\lambda - c'$ must have three real roots alternating in sign, for Turing instability to occur and $d' > 0$ is a necessary condition for Turing-Hopf instability.*

Proof. It is well-known that there are either four distinct real roots or four distinct complex roots when $\Delta_4 > 0$, two real and two complex roots when $\Delta_4 < 0$, and duplicate roots when $\Delta_4 = 0$. Assuming $\Delta_4 > 0$, all roots must be real for Turing instability to occur. By Rolle's theorem, there must be a real value between each pair of roots where $r(\lambda)$ has slope 0 at that point, and these values must be alternating in sign because no roots are repeated. Thus, $r'(\lambda) = 4\lambda^3 - 3a'\lambda^2 + 2b'\lambda - c'$ must have three real roots alternating in sign.

Assuming $\Delta_4 > 0$, we must have four complex roots for Turing-Hopf instability to occur. Let these roots be $w + xi$, $w - xi$, $y + zi$, and $y - zi$. Thus, we have $d' = (w^2 + x^2)(y^2 + z^2) > 0$. ☐

VI. PATTERN FORMATION

Many epidemics are comprised of waves of infections. Here, we aim to simulate such waves by adding stochastic noise to an initial steady state, which creates spatial oscillations. In a physical sense, this noise can represent fluctuations in infections that are induced by changes in external dynamics such as weather. We shall dedicate this section to analyzing simulation results with the proposed **MBRD-SI** and **MBRD-CI** models. Particularly, in Subsection VI A, we describe the methodology for our experiments. In Subsection VI B, we analyze two examples of pattern formation. In Subsection VI C, we aim to understand the effect of different parameters on hotspot growth. Finally, in Subsection VI D, we explore the effect of variations in layerwise network degrees on pattern formation and growth.

A. Methodology

Because infection densities cannot be negative in the real world, we set 0 as the minimum threshold for all densities. We conduct simulations on three types of networks:

- **Lattice networks.** With simulations on lattice networks, we can more easily view patterns that form. We implement the LA4, LA12, and LA24 lattice networks, in which most nodes have degree 4, 12, and 24, respectively. These are represented in Figure 8. In each of the lattices in the figure, the center red vertex is connected to the green vertices through edges. Lattice networks have a deterministic structure and give us identical solutions across trials.

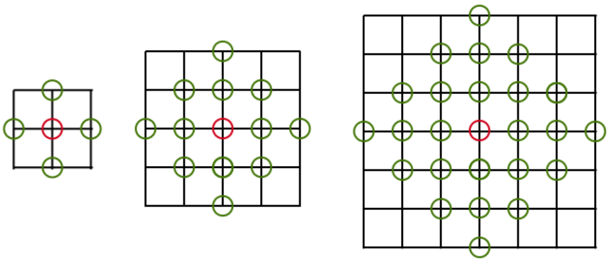

FIG. 8: The LA4 (left), LA12 (middle), and LA24 (right) networks.

- **Watts-Strogatz (WS) network.** The Watts-Strogatz model [42] is characterized by short geodesic distances between nodes; this phenomenon is called the small-world effect. Thus, diffusion on small-world networks is faster than diffusion on other networks such as lattice networks.
- **Barabási-Albert (BA) network.** The BA network [43] is a scale-free network and follows a power-law degree distribution. It also incorporates preferential attachment, meaning that each node is more likely to create new connections if it already is connected to many other nodes.

We simulate with the WS and BA networks because both the small-world phenomenon and scale-free properties are present in social networks [43, 44], the World Wide Web [45, 46], and migration between physical human communities [47, 48]. We consider the following metrics throughout this section:

Definition 4 (Pattern amplitude for superinfection dynamics)**.** The amplitude of the densities among all layers of the multiplex network in superinfection dynamics is

$$A := \sqrt{\sum_{i=1}^{N} [(S_i - S^*)^2 + (I_i - I^*)^2 + (J_i - J^*)^2]}, \quad (23)$$

where S^*, I^*, and J^* are the equilibrium densities for the susceptible, pathogen 1-infected, and pathogen 2-infected populations.

Definition 5 (Pattern amplitude for co-infection dynamics)**.** In co-infection dynamics, the amplitude A is defined as

$$\sqrt{\sum_{i=1}^{N} [(S_i - S^*)^2 + (I_i - I^*)^2 + (J_i - J^*)^2 + (C - C^*)^2]}, \quad (24)$$

where S^*, I^*, J^*, and C^* are the equilibrium densities for the susceptible, pathogen 1-infected (mono- or co-infected), pathogen 2-infected populations, and co-infected populations.

There are some co-infection patterns that revolves around different densities than the original equilibrium. In that case, we use the following alternate definition of A from Equation (23):

$$\sqrt{\sum_{i=1}^{N} [(S_i - \bar{S})^2 + (I_i - \bar{I})^2 + (J_i - \bar{J})^2 + (C - \bar{C})^2]}, \quad (25)$$

where $\bar{S}$, $\bar{I}$, $\bar{J}$, and $\bar{C}$ are the mean densities of all nodes in the network: $\bar{S} = \sum_{i=1}^{N} S_i$, $\bar{I} = \sum_{i=1}^{N} I_i$, $\bar{J} = \sum_{i=1}^{N} J_i$ and $\bar{C} = \sum_{i=1}^{N} C_i$.

B. Amplifying Hotspots

Emerging spatial hotspots have been investigated in the spread of COVID-19 [49]. Here, we focus on hotspots that arise from Turing instability. In SIS dynamics, prior research has shown that Turing patterns often become spatiotemporally stationary after a period of time [21]. Meanwhile, in both the **MBRD-SI** and **MBRD-CI** dynamics discussed in this paper, we find that it is possible for these peaks to be both spatially stationary while also consistently growing over time until system collapse occurs. We illustrate this phenomena with Examples 1 and 2 for superinfection and co-infection dynamics, respectively.

Example 1 (**MBRD-SI** model)**.** Consider the **MBRD-SI** model in Equation (3) with the following parameters:

$$\begin{aligned}
&\mu = 0.005, && r = 0.1, && A = 0.1, && K = 1,\\
&\beta_1 = 0.3, && \beta_2 = 0.15, && \sigma = 3, &&\\
&\gamma_1 = 0.02, && \gamma_2 = 0.05, && \alpha_1 = 0.02, && \alpha_2 = 0.15,\\
&d_{11} = 0.1, && d_{12} = -0.2, && d_{13} = -0.2, &&\\
&d_{22} = 0.01, && d_{33} = 4.8. && &&
\end{aligned} \quad (26)$$

On a multiplex network with three identical LA12 networks for the S, I, and J layers, the configuration in Example 1 forms the patterns in Figure 9. This figure demonstrates the layers with S, I, and J densities, in order of row, at times $t = 500$, 1300, and 1850, respectively. As seen in the figure, we observe the emergence and growth of patterns with dots and stripes in the S and I layers. In those layers, the hotspots are still at the same locations between times 500 and 1300, which is a key features of Turing patterns. On the other hand, pattern formation does not occur on the J layer, demonstrating the possibility that Turing patterns occur only on some layers and not all of them. Finally, we notice from Figure 9 that the I layer densities are centered around approximately 0.52 and the J layer densities are centered around approximately 0.4. This shows that it is possible for the I layer to have a greater equilibrium even when J steals hosts from I, and this is largely because of β_1 being significantly larger than β_2.

From our derivations, we expect that the type of network should not affect whether or not pattern formation occurs as long as the average degrees are constant, especially when the average degrees of each layer are large. We observe that this is indeed true for the **MBRD-SI** dynamics described in Equation (3) and Example 1. The MBRD-SI model, with the parameters mentioned above, produce patterns in LA4-LA4-LA4 networks. Figure 10 displays the oscillating node densities at $t = 100$ with the superinfection model parameters in Example 1 on a WS multiplex network on the same multiplex network.

We introduce a co-infection parameter setting below, which produces patterns with very similar shapes to that of Example 1.

Example 2. [**MBRD-CI** model] Consider now the **MBRD-CI** model in Equation (4) and the following parameter settings in Example 2:

$$\begin{aligned}
&\mu = 0.005, && r = 0.1 && A = 0.1, && K = 1,\\
&\beta_1 = 0.3, && \beta_2 = 0.15, && &&\\
&\beta_{10} = 0.1, && \beta_{02} = 0.1, && \beta_{12} = 0.05, &&\\
&\gamma_1 = 0.02, && \gamma_2 = 0.05, && &&\\
&\alpha_1 = 0.02, && \alpha_2 = 0.15, && \alpha_{12} = 0.1, &&\\
&d_{11} = 0.4, && d_{12} = -0.2, && d_{13} = -0.2, &&\\
&d_{22} = 0.01, && d_{33} = 4.8. && &&
\end{aligned} \quad (27)$$

On a multiplex network with three identical LA4-LA4-LA4 networks for the layers with S, I, J densities, this configuration forms the patterns in Figure 11. This figure

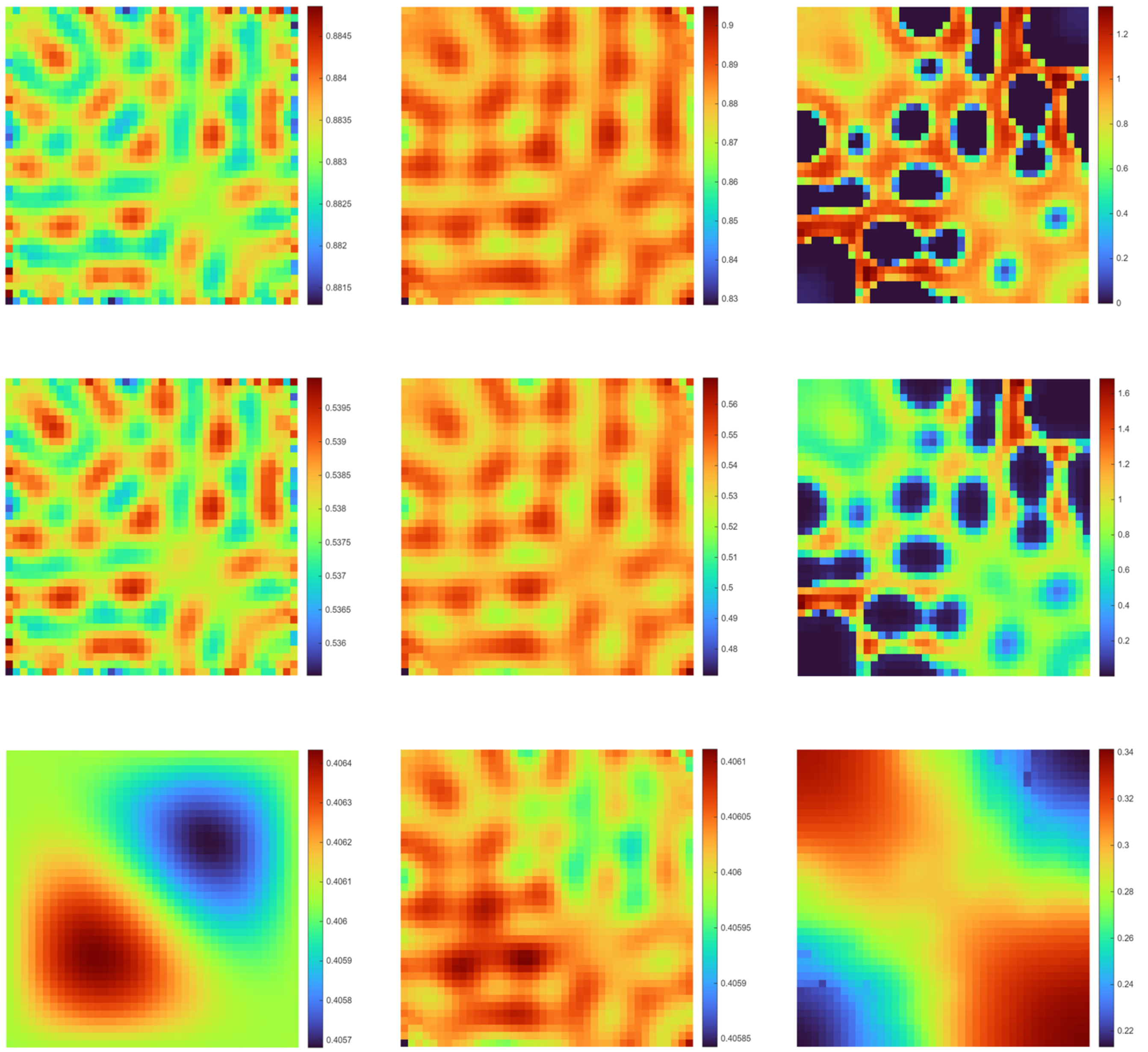

FIG. 9: Spatial distribution of susceptible (first row), pathogen 1 infection densities (second row), and pathogen 2 infection densities (third row). For each, plots are displayed for $t = 500$ (first column), $t = 1300$ (second column), and $t = 1850$ (third column).

presents the the four layers, in order of row, at times $t = 300$, 500, and 700, respectively. We observe fine-grained Turing patterns with a labyrinth structure, and the hotspots are still at the same locations between times 300 and 500.

System collapse as a result of growing Turing patterns has been investigated in competition dynamics between pathogens [50]. We see the same phenomenon occur in both **MBRD-SI** and **MBRD-CI** dynamics. From the first and second columns of Figure 9, the oscillations increases until a time around $t = 1600$ when system collapse begins, as shown in the third column of Figure 9. The system collapse can be seen in the fading of the pattern in Figure 9 because many nodes reach 0 and stay there. We also see the oscillations amplify in the first two columns of Figure 11, as well as system collapse in the third column. This demonstrates that with the right parameter settings, it is possible for both the human population and strains to disappear in most nodes. Thus, local oscillations can cause local system collapse, which

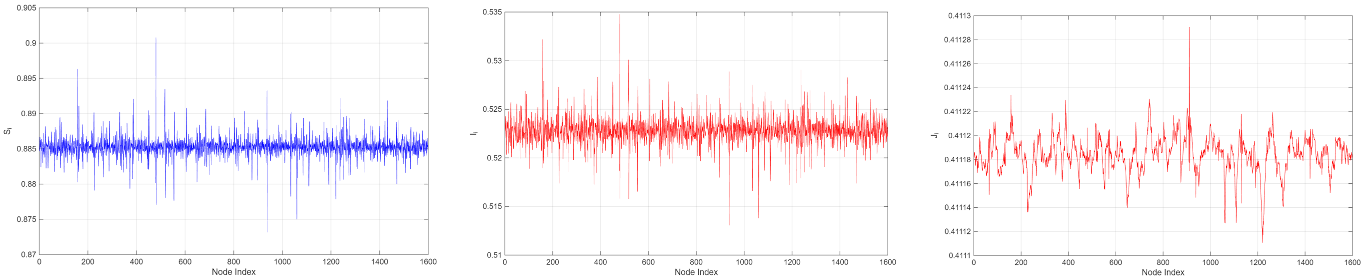

(a)

(b)

(c)

FIG. 10: Spatial distribution of densities on each layer at time $t = 100$ on an WS multiplex network with all layers having average degree of 4.

propagates to other areas and leads to global collapse.

Overall, from observation, we find Turing-Hopf patterns are rarer than Turing patterns. With the presence of Turing patterns, location-targeted intervention will be easier as the hotspots formed are stationary. With Turing-Hopf patterns, the locations most in need of intervention will constantly be changing, making an effective response more difficult.

C. Effects of Model Parameters

In this subsection, we aim to understand the effect of various model parameters on pattern formation and the growth of Turing instability-induced hotspots.

We find that the following characteristics are present in most of the patterns we have studied and thus, we believe they help induce pattern formation.

- There is a significant difference between the transmission rates β_1 and β_2 and the virulences α_1 and α_2. This is especially true for the **MBRD-SI** model.
- The cross-diffusion rates d_{12} and d_{13} are negative, meaning in the physical sense that susceptible individuals gravitate towards areas with a high number of infections of either pathogen.
- There is a substantial difference between at least two of the diffusion rates d_{11}, d_{22}, and d_{33}. We see that this is true in the parameter settings shown in the last seciton. This is also consistent with the parameter settings for the patterns described in [20, 21].

We observe through our scenario that increasing σ inhibits pattern growth; an example can be seen in Figure 20, which is based on the parameter setting in Example 1 and the superinfection model in Equation (3). We observe that the relationship between the average amplitude at $t = 50$ can be described by a power curve, as described in the caption of Figure 20. As a result, larger σ will make it less likely for the pattern to evolve back into the steady-state and system collapse to occur more quickly. Thus, in this case, a greater superinfection coefficient is most favorable in the long-term.

We consider the **MBRD-CI** dynamics from the model in Equation (4). We note that in many scenarios, the majority of amplitude growth originates from fluctuations between nodes in mono-infections in co-infection dynamics. We use the configuration in Example 2, except for the co-transmission coefficient β_{12}, which we vary. From Figure 13, we see that the average amplitude peaks approximately when $\beta_{12} = 0.2$. We fit the resulting points with a Fourier series, and the curve's formula is shown in Figure 13.

This further analysis highlights the dual role of the co-transmission coefficient. Small values of β_{12} are insufficient to sustain strong co-infection clusters, while very large values rapidly homogenize the system and suppress pattern formation. The intermediate regime (around $\beta_{12} = 0.2$) maximizes oscillations, suggesting that there exists a critical threshold at which co-infections amplify spatial heterogeneity most strongly. In our setting, it implies that targeted interventions which reduce co-transmission could substantially weaken pattern growth and delay system collapse.

D. Varying Network Degrees

We shall dedicate this section to analyzing the effect of varying average degrees between layers on pattern formation and growth. We mainly analyze this from the standpoint of clustering, which influences how difficult a disease is to mitigate.

We analyzed the coinfection pattern with 8 combinations of varying networks: (LA4, LA4, LA4), (LA12, LA12, LA4), (LA12, LA4, LA4), (LA12, LA4, LA12), (LA12, LA12, LA12), (LA24, LA12, LA4), (LA24, LA4, LA12), (LA24, LA24, LA24). Figure 14 presents patterns in the I and C layers (first and second rows) for varying degree layers at time 100 for the **MBRD-CI** dynamics in Equation (4) and Example 2 for the other three pattern-forming layer combinations besides (LA4, LA4, LA4). The I and C layers are pictured in the first and second rows, respectively. Additionally, the first, second, and third columns depict pattern formation for the

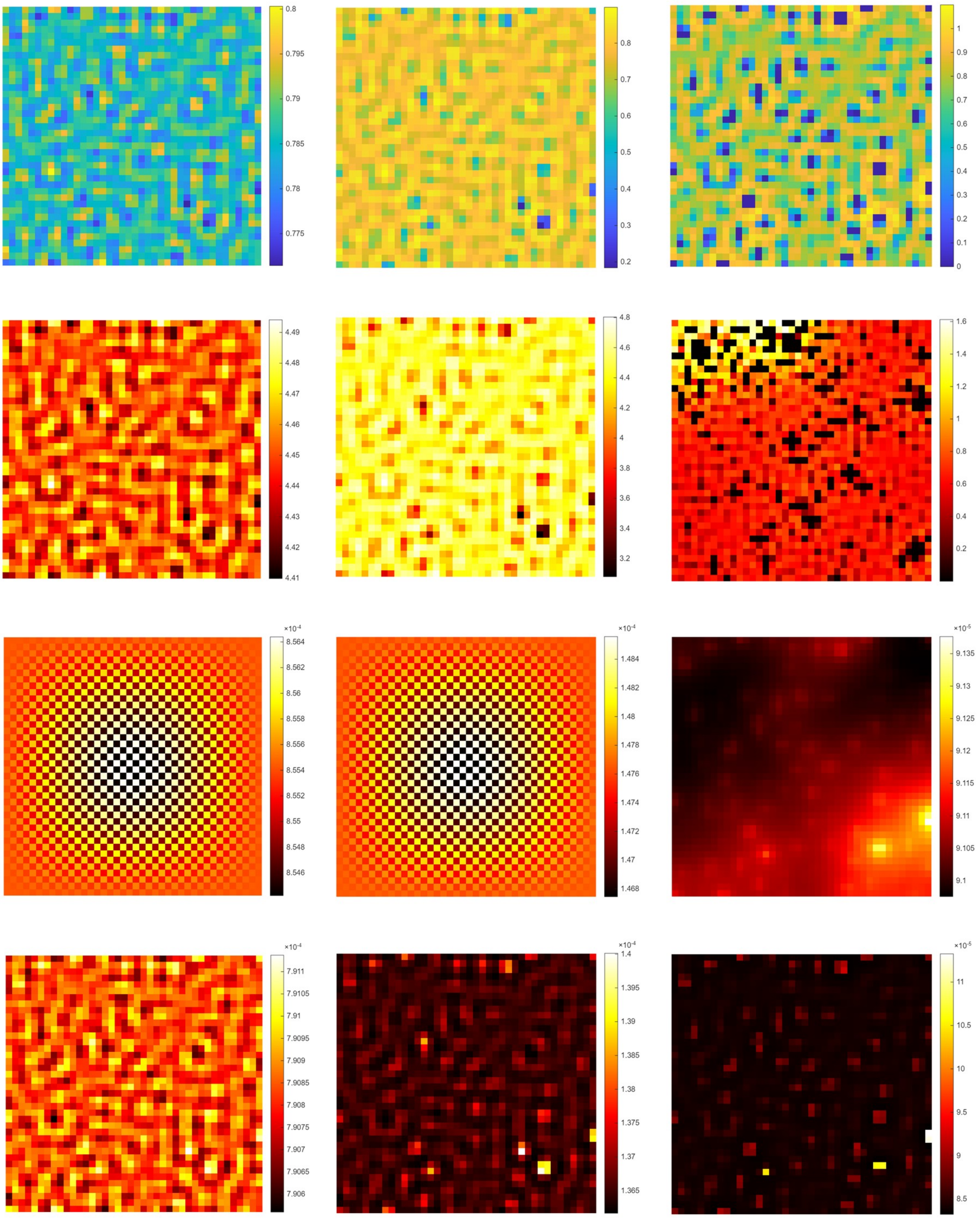

FIG. 11: Spatial distribution of susceptible (first row), pathogen 1 infection densities (second row), pathogen 2 infection densities (third row), and co-infection densities (fourth row) on a LA4-LA4-LA4 network at $t = 300$ (first column), $t = 500$ (second column), and $t = 700$ (third column).

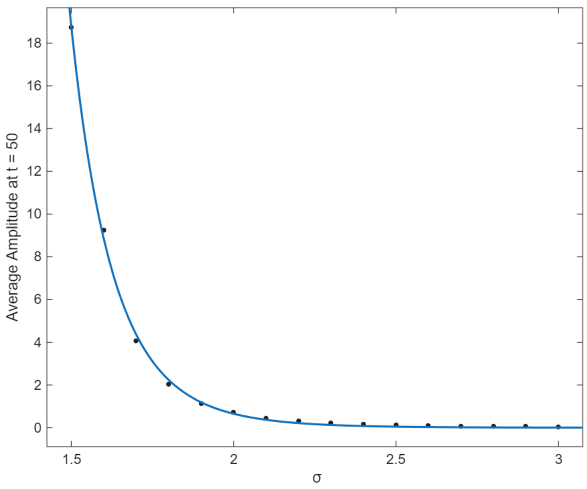

FIG. 12: Amplitude at $t = 50$ (average of five trials) for varying σ values on a LA4-LA4-LA4 network, based on Example 1. Fitted curve: $y = a \cdot x^b$ where $a = 2141.6$ and $b = -11.6768$.

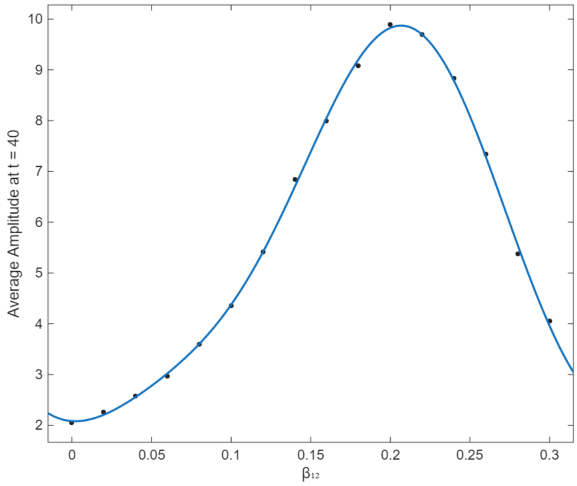

FIG. 13: Amplitude growth of oscillations for different β_{12} values on a LA4-LA4-LA4 network at $t = 40$, based on Example 2. Fitted curve: $y = a_0 + a_1 \cos(xw) + b_1 \sin(xw) + a_2 \cos(2xw) + b_2 \sin(2xw)$, where $a_0 = 5.4740$, $a_1 = -3.4742$, $b_1 = -1.4995$, $a_2 = 0.0836, 0.6879$, $w = 17.8057$.

(LA12, LA12, LA4), (LA12, LA12, LA12), and (LA24, LA24, LA24). We make the following observations and illustrate them with Figure 14.

- It was previously mentioned that pattern formation occurred in four combinations out of the configurations analyzed: (LA4, LA4, LA4), (LA12, LA12, LA4), (LA12, LA12, LA12), and (LA24, LA24, LA24). Pattern formation occurred exactly for those combinations also with the superinfection example. We notice that pattern formation occurs more often when the layers have the same degrees. Because infection hotspots are difficult to mitigate, it is ideal for variation to occur between layers. Longer quarantine periods and limits on migration for infected populations would induce large average degree variations between the layers, preventing Turing patterns from forming.
- Zhao *et al.* emphasized that increasing layerwise average degrees can lead to larger clusters [21]. This also occurs in our simulation and is illustrated in Figure 14, where the clusters for (LA24, LA24, LA24) are the largest and there are only small clusters at the early stages for (LA4, LA4, LA4). Because larger clusters of hotspots are more difficult to mitigate, it is beneficial to limit migration for all individuals while limiting migration for infected individuals to a greater extent.

VII. POINT-SOURCE INFECTIONS

Many epidemics, such as the COVID pandemic, originate in a single location. In this section, we explore superinfection and co-infection dynamics after both are introduced at different nodes. In particular, we aim to understand the effects of the infection source locations, time difference of pathogen introductions, and the superinfection and co-infection parameters on the infection spread. Finally, we consider the impact of different network topologies and varying average layer degrees on infection spread.

A. Methodology

We let I_0 and J_0 be the initialized source nodes for pathogen 1- and pathogen 2-infections, respectively. We introduce the following terminology and metrics:

Definition 6. We call a node I_1-*active* (resp. I_2-*active*) if its density of I_1-infections (resp. I_2-infections), including only mono-infections, is greater than I_{thres} (resp. J_{thres}). We call a node C-*active* if the density of co-infections is greater than C_{thres}.

Definition 7. We define the I_1-*spread index* (resp. I_2-*spread index*) to be the fraction of nodes that are I_1-active (resp. I_2-active). Additionally, we define the C-*spread index* to be the fraction of nodes that are C-active.

In this paper, we set $I_0 = J_0 = 0.05$, $I_{thres} = J_{thres} = 0.01$ for both superinfection and co-infection simulations. We also define $C_{thres} = 0.005$ for the co-infection simulations. We also introduce the following definitions, which will be useful in Subsection VII F.

Definition 8 (Peaks)**.** Let $\delta(t)$ be the I_1-, I_2- or C-spread index as a function of the time t. For some integer time increment τ, we define a *local peak time* $t^* > 0$ to be integer multiple of τ that satisfies

$$\delta(t^* - \tau) < \delta(t^*),$$

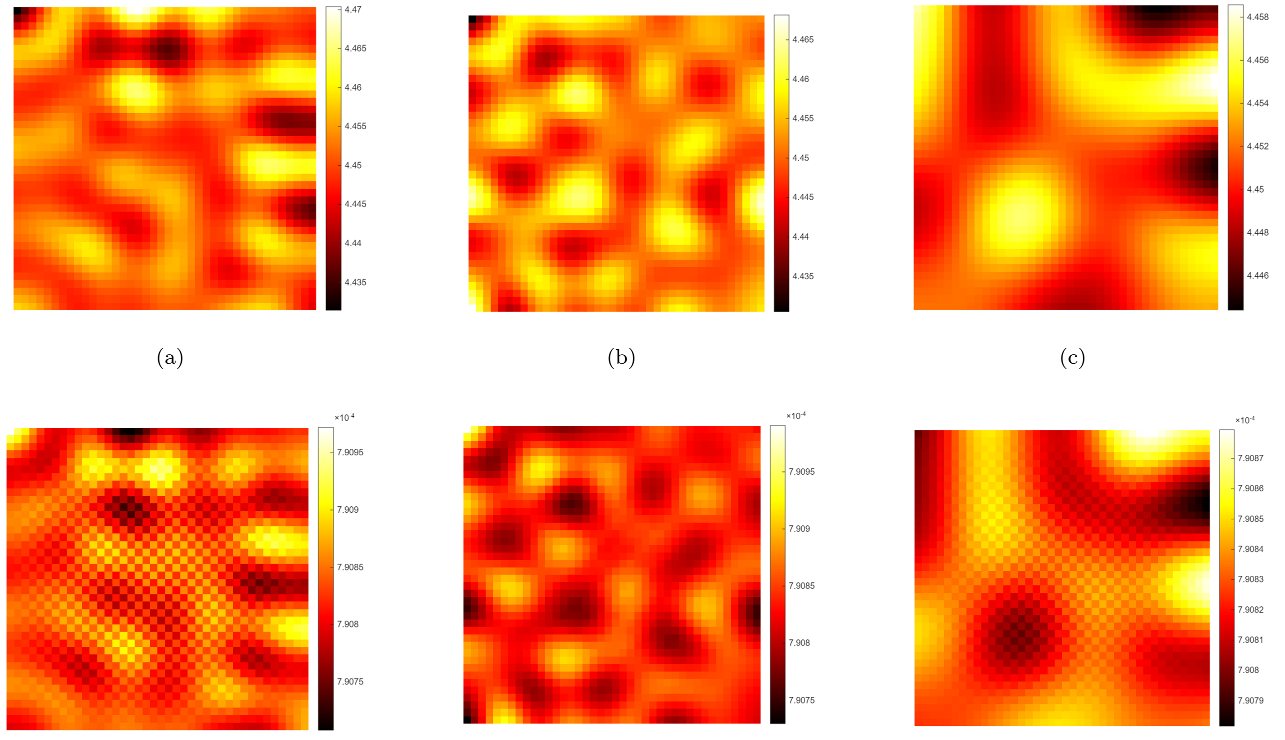

(a) (b) (c)

(d) (e) (f)

FIG. 14: Layers with I (top row) and C densities (bottom row) for three multiplex networks: LA12-LA4-LA4 (first column), LA12-LA12-LA12 (second column), and LA24-LA24-LA24 (third column).

under the condition that there exists an integer u such that $u \equiv 0 \bmod \tau$, $u \geq t^*$, $\delta(u) > \delta(u+\tau)$, and

$$\delta(t) = \delta(t^*) \ \forall \ t \in \{(t^*, u] \mid t \equiv 0 \bmod n\}.$$

We also define the corresponding *peak value* to a local peak time t^* as $\delta(t^*)$. Additionally, for a local peak time t^*, we define the corresponding *peak* to be $\delta(t^*)$. Furthermore, we define the *n-th peak time* to be the unique time t_n such that there exist exactly $n-1$ local peak times less than t^*, and the *nth peak value* to be $\delta(t_n)$.

Definition 9 (Saturation time)**.** For time-increment τ and $\delta(t)$ as a spread index as a function of t, we define the *saturation time* of a spread index to be an smallest integer multiple of τ, t^*, such that $\delta(t^*) = 1$.

In our simulations, we use a time increment of $\tau = 1$. Using a larger τ would provide smoother spread-index graphs. Finally, to illustrate our observations in the following subsections, we introduce the following superinfection parameters for Equation (3), and co-infection parameters for Equation (4).

Example 3. (Superinfection model)

$$\begin{array}{llll} \mu = 0.005, & r = 0.1, & A = 0.1, & K = 1 \\ \beta_1 = 0.5, & \beta_2 = 0.4, & \sigma = 0.9, & \\ \gamma_1 = 0.2, & \gamma_2 = 0.1, & \alpha_1 = 0.01, & \alpha_2 = 0.05, \\ d_{11} = 0.3, & d_{12} = 0.1, & d_{13} = 0.1, & \\ d_{22} = 0.3, & d_{33} = 0.1. & & \end{array} \tag{28}$$

Example 4. (Co-infection model)

$$\begin{array}{llll} \mu = 0.005, & r = 0.1, & A = 0.1, & K = 1, \\ \beta_1 = 0.3, & \beta_2 = 0.4, & & \\ \beta_{10} = 0.2, & \beta_{02} = 0.3, & \beta_{12} = 0.05, & \\ \gamma_1 = 0.1, & \gamma_2 = 0.05, & & \\ \alpha_1 = 0.05, & \alpha_2 = 0.15, & \alpha_{12} = 0.25, & \\ d_{11} = 0.3, & d_{12} = 0.1, & d_{13} = 0.1, & \\ d_{22} = 0.3, & d_{33} = 0.1. & & \end{array} \tag{29}$$

In Subsection VII B, we discuss the overall shape of the spread index evolutions. In Subsection VII C and VII D, we evaluate the impact of the distance and time difference, respectively, between the initialization of pathogen 1 and 2. In Subsection VII E, we discuss the impact of superinfection or co-infection model-specific parameters. Finally, in Subsection VII F, we evaluate the impact of different network types and average layer degrees on the spread of infections in this context.

B. Nature of Infection Dynamics

Consider the superinfection model in Equation (3). In many scenarios with superinfection dynamics, we expect the eventual persistence of pathogen 2 infections in every region and pathogen 1 infections to die out as a result of pathogen 2's ability to steal hosts. We see that this is true for the parameter set in Example 3 with the top row in Figure 15. In many cases, the I_1-spread index experiences a single peak and falls back to 0. Meanwhile, the I_2-spread index eventually becomes 1, as shown in Figures 15 and 16.

In the co-infection dynamics shown in Equation (4), it is less likely for one pathogen to completely dominate the other. Thus, we expect that in some scenarios, both the I_1-, I_2-, and C-spread indexes will reach 1 over time. We see in Figure 17 that it is possible for that to occur. Moreover, it is possible for one pathogen to dominate over the other, causing one mono-spread index to peak and fall back to 0 and the other mono-spread index to persist at 1 as shown in Figure 21 when $\beta_{12} = 0.01$.

C. Effect of Source Locations

We first focus on the effect that source locations for both pathogens have on the spread of both pathogens throughout networks. For simplicity, we perform our simulations with 40×40 lattice networks. We denote d_{ij} to be the starting path distance between the sources of pathogen 1 and pathogen 2.

With respect to location, we focus on two configurations. The first, as seen in Figure 15(a), features pathogen 1 originating from the center of the network with initial density 0.05. At the same time $t = 0$, we let pathogen 2 originate at j_1, j_2, j_3, or j_4, which are ordered based on distance from node i. We analyze this scenario for both superinfection dynamics (see Figure 15) and co-infection dynamics (see Figure 17).

Considering Example 3 and the superinfection model in Equation (3), we believe it is reasonable to expect that for both pathogen dynamics, the weaker pathogen's spread index peaks at a greater value or the time for that pathogen's spread index to reach 1 decreases as the distance between the source locations of pathogens 1 and 2 increases. This is because pathogen 1 has time to dominate a large area before both pathogens start to compete in the same locations. We observe from both figures that this is indeed true. However, in this specific configuration, we note that the initial distance between the pathogen sources has a minimal impact on the time at which the I_1-spread index peaks in the superinfection dynamics in Figure 15(b).

For the same initialization configuration but with the co-infection dynamics in Equation (4), we first note that as d_{ij} increases, one of the I_1-spread index or I_2-spread index reaches 1 earlier while the other reaches 1 later. For Example 4, pathogen 2 has higher transmission rates than pathogen 1. The I_1-spread index reaches 1 at an earlier time and the I_2-spread index reaches 1 at a later time because the I_1-spread index has more room to grow before the pathogens start interacting. We also find that the C-spread index reaches 1 at a later time as d_{ij} increases. This could be investigated in a future study.

The second initialization configuration, pictured in 16(a) for the superinfection dynamics in Equation (3) with Example 3, features pathogen 1-infections originating from a corner of the lattice, while the origin of pathogen 2-infections varies. We observe that the source location for pathogen 2 has a more irregular impact on the I_1-spread index's peak. The largest peaks occurs when pathogen 2 is initialized at j_1 and j_4. This can be explained by the overall direction in movement of both infection spreads. When pathogen 2 is initialized at j_4, the I_1-spread index has more room to grow before both pathogen infections start diffusing at the same locations. On the other hand, when the origins of pathogen 1 and 2 are close, pathogen 1 more easily catches up to the places that pathogen 2 is infecting already before pathogen 2 infections can grow significantly. It is surprising that the initializations at j_2 and j_3 produce the smallest peaks by a large margin, even though j_1 is fairly close to j_2 and j_3 is close to j_4.

Because pathogen 2 is dominant and has a higher virulence α_2, it is most ideal for the J-spread index to grow slowly. We see from the superinfection examples that the I_2-spread index grows relatively slowly when the pathogens originate a far distance from each other, assuming the initialization in Figure 15(a) or Figure 16(a). For co-infection dynamics, if we seek to slow the spread of the infection that has the greatest virulence, different configurations are most beneficial depending on the nature of each infection. In this case, the co-infected group has the greatest virulence of 0.25. Thus, it is most ideal for the distances between the pathogen initializations to be as far as possible, assuming the configuration in Figure 15(a).

D. Effect of Source Time Differences

In this subsection, we investigate the impact of time differences in the introduction of the two pathogens in the network, where pathogen 2 infections are introduced some time after pathogen 1 infections. We denote the time difference between the introductions of pathogens 1 and 2 in the network to be t_d. For superinfection dynamics, we expect that pathogen 1 infections will have more time to spread to a greater area before superinfection occurs at a large rate. We see this is true when we incorporate the parameter values from Example 3 with the model in Equation (3) and initialize pathogen 1- and pathogen 2-infections to originate at opposite corner nodes in a 1600-node lattice network. In Figure 18, we observe that as the time difference t_d of the introduction of the two pathogens-induced infections increases, both

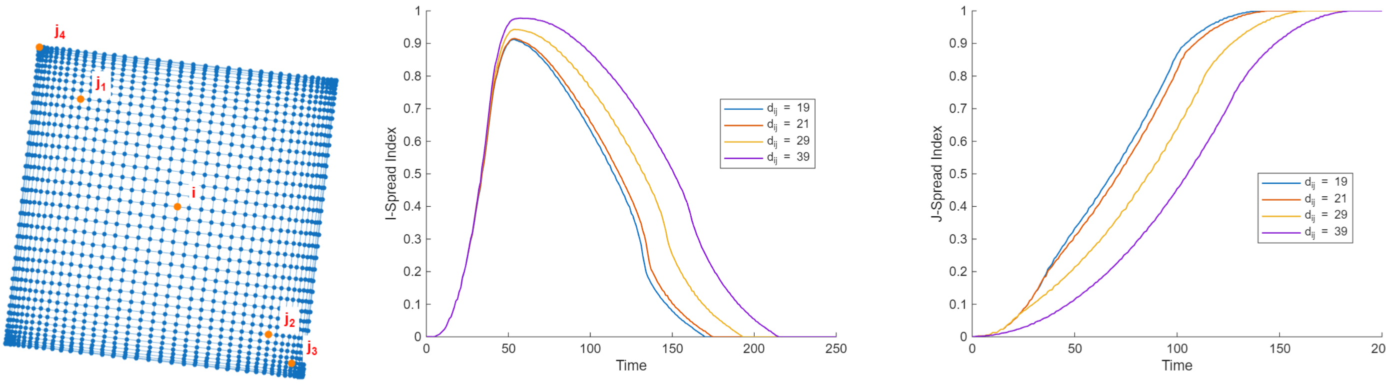

(a) (b) (c)

FIG. 15: I_1-spread index (center) and I_2-spread index (right) when I is introduced in a central location and the starting location of J varies (left). Based on Example 3.

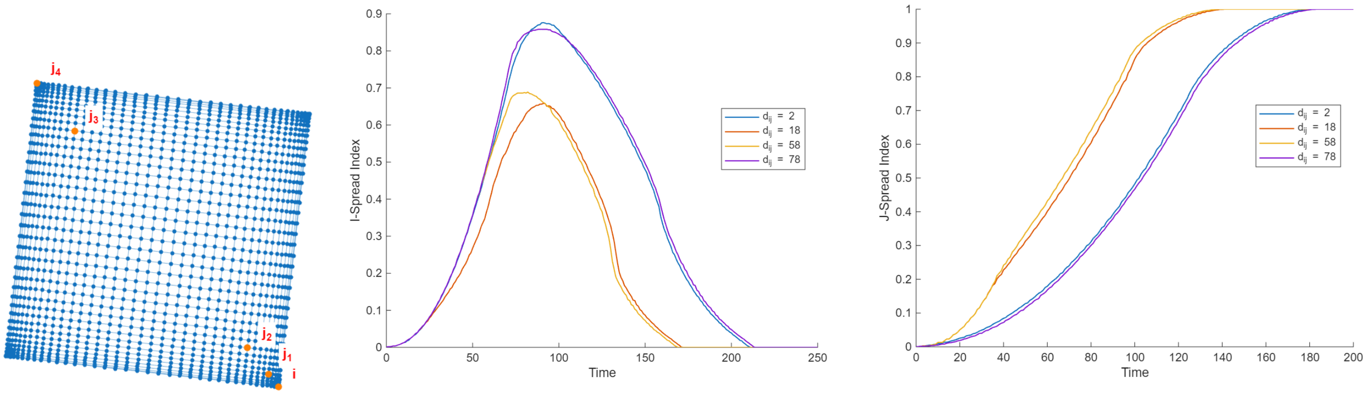

(a) (b) (c)

FIG. 16: I_1-spread index (center) and I_2-spread index (right) when pathogen 1 is introduced in a central location and the starting location of pathogen 2 varies (left). Based on parameter configuration in Example 3.

the peak I-spread index and the time that this peak occurs will increase. The progression of the I_1-peak value follows approximately a power curve, and the progression of the I_2-saturation time as a linear relationship with the time t_d.

We keep the same settings as before, but incorporate the coinfection model from Equation (4) and the co-infection parameters from Example 4. Again, we see that one mono-infection spread index reaches 1 sooner as t_d increases, and the other spread index reaches 1 at a later time, from Figure 19. Moreover, we see for both peaks that the time at which the peaks occur both shift forward as t_d increases. We observe that for both in Figure 17 and the evolution of the I_1- and I_2- spread indexes over time for the current example, the C-spread index follows the same trend in response to location or time changes as the I_2-spread index. We believe this could be true in general co-infection dynamics and propose this as an interesting topic of future study.

E. Effect of Superinfection and Co-Transmission Parameters

Because a larger superinfection coefficient σ allows pathogen 2 to dominate more easily, we expect that as σ increases, the I_1-spread index will peak at a lower value and at an earlier time. This is because the I_1-spread index will have less room to grow before it becomes significantly dominated by pathogen 2-infections and falls back to 0 when pathogen 2 is more dominant. We verify these statements with the model in Equation (3) and the parameter settings in Example 3, with varying values of σ. In Figure 20, we observe that as σ increases, the I_1-peak value and I_2-peak time both decrease, and the relationship can be fitted to a power curve, respectively. Moreover, the I_2-saturation time decreases according to a power-curve relationship. Because the correlations are all negative, it is most ideal for the superinfection coefficient to be small.

For co-infection dynamics in Equation (4), we expect that as β_{12} increases, the probability that an individual

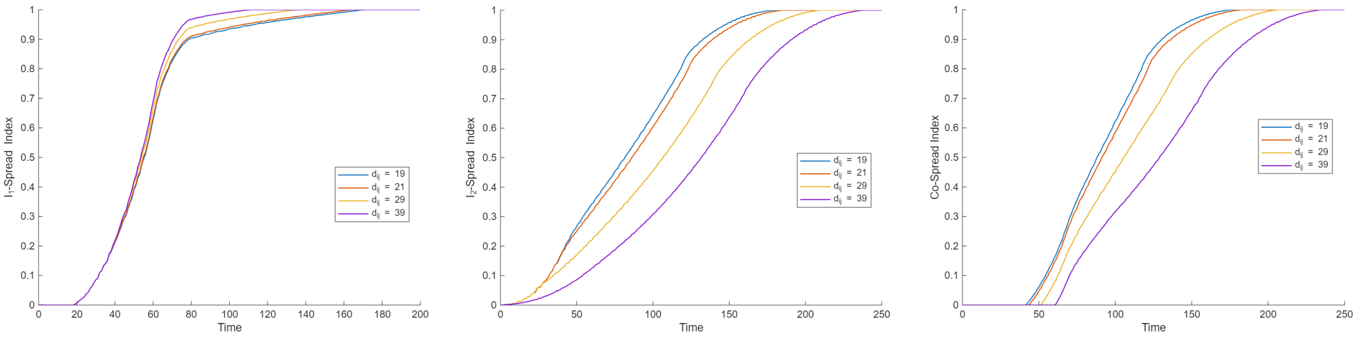

(a) (b) (c)

FIG. 17: I_1-, I_2-, and C-spread indexes for both pathogens over time when pathogen 1 is introduced in a central location and the starting location of pathogen 2 varies. Based on Figure 15(a) and Example 4.

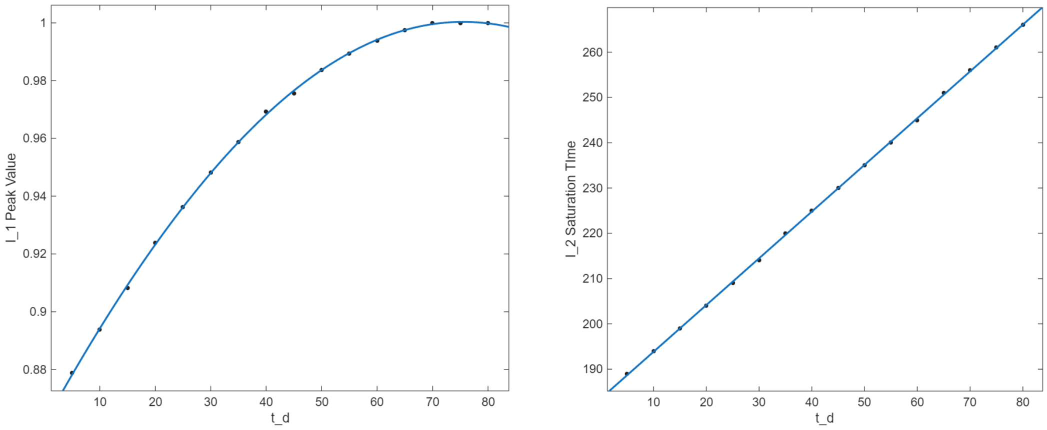

(a) (b)

FIG. 18: I_1-peak value (left) and I_2-saturation time (right) as t_d varies. Left fitted curve: $y = a_0 + a_1 \cos(xw) + b_1 \sin(xw)$, where $a_0 = 0.548$, $a_1 = 0.3131$, $b_1 = 0.3264$, and $w = 0.0107$. Right fitted curve: $y = ax + b$, where $a = 1.0318$, $b = 183.5250$.

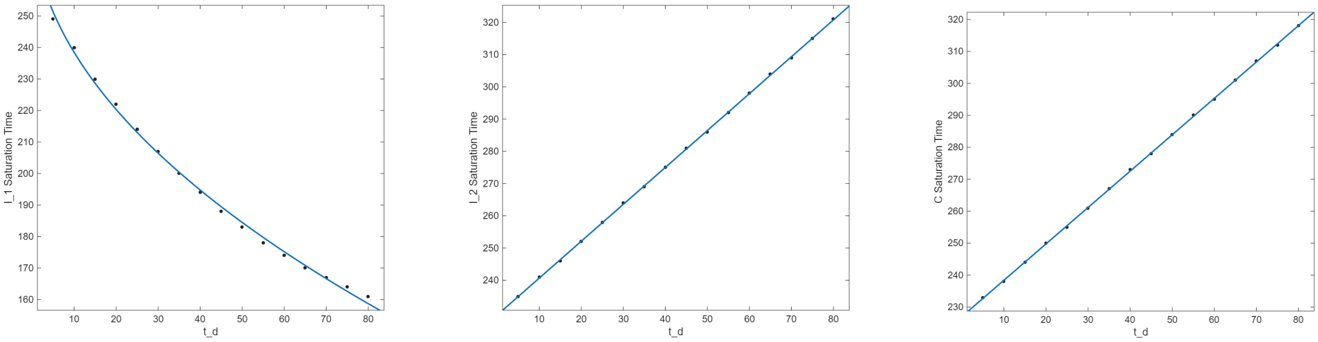

(a) (b) (c)

FIG. 19: Saturation times of I_1 (left), I_2 (center), and C (right) with varying t_d. Based on Example 4, I is introduced at node 1, and J is introduced at node 1600. Left fit curve: $y = ax^b + c$, where $a = -14.071$, $b = 0.4964$, and $c = 282.6$. Center fit curve: $y = ax + b$, where $a = 1.1441$ and $b = 229.25$. Right fit curve: $y = ax + b$, where 1.1382 and $b = 227$.

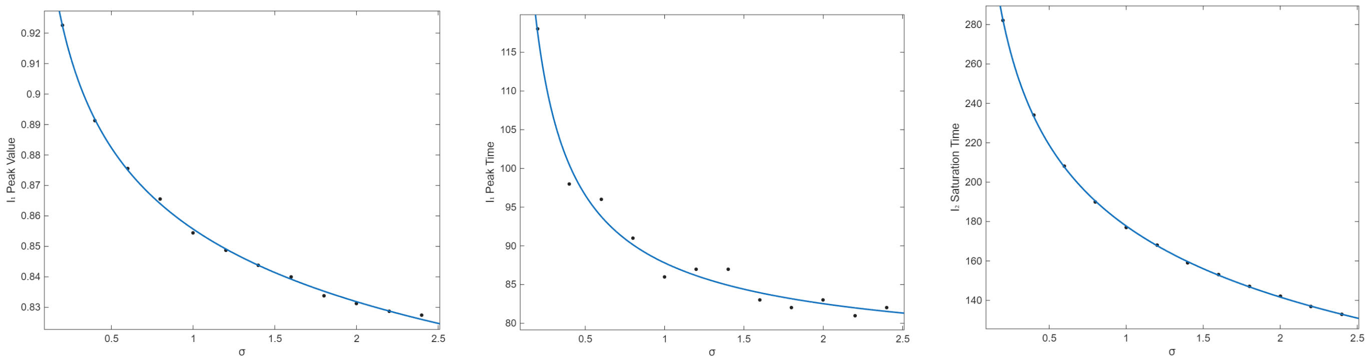

(a) (b) (c)

FIG. 20: I_1-peak value (left), I_1-peak time (center), and I_2-saturation time (right) over varying σ. Left fitted curve: $y = ax^b + c$, where $a = 0.2239$, $b = -0.1624$, and $c = 0.6318$. Center fitted curve: $y = ax^b + c$, where $a = 13.285$, $b = -0.73$, and $c = 74.521$. Right fitted curve: $y = ax^b + c$, where $a = 293.11$, $b = -0.1895$, and $c = -115.36$.

will be co-infected will increase, resulting in the C-spread index reaching 1 sooner. We see this occurs in Figure 21, which was created using the parameter set from Example 4. From this figure, we also note that the dynamics when $\beta_{12} = 0.01$, 0.05 and 0.09 can be described as mutual inhibition, while the dynamics when $\beta_{12} = 0.14$ can be described as mutual enhancement. We observe that all three indexes reach 1 earlier when mutual enhancement occurs.

In this figure, we observe that $\beta_{12} = 0.14$ allows all three indexes to reach 1 at the earliest times, and $\beta_{12} = 0.01$ enables the I_1-spread index and C-spread index to peak and then fall to 0. This inspires the following definition:

Definition 10 (β_{12} threshold)**.** We define the β_{12} threshold of a co-infection parameter configuration to be the largest value of β_{12}, with all other parameters fixed, such that the maximum C-spread index over time is less than 1 and converges to 0.

When the co-infection removal rate α_{12} is large, we expect that the value of β_{12} must make up for it, and the β_{12} threshold must be larger. From Figure 22, we observe that the relationship between the β_{12} threshold and the value of α_{12}. We believe that proving this relationship mathematically would be an interesting subject of future work.

F. Effect of Network Type and Layer Degrees

Investigating the impact of varying network types and layer average degrees is highly useful in understanding infection spread and effective public health policy. We analyze infection spreading in LA, WS and BA networks and with 8 different combinations of average layer degrees. We analyze these factors with the following superinfection and co-infection parameter sets, as well as Examples 3 and 4.

Example 5 (Superinfection model)**.**

$$\begin{array}{cccc} \mu = 0.005 & r = 0.1 & A = 0.1 & K = 1 \\ \beta_1 = 0.3, & \beta_2 = 0.5, & \sigma = 1.2 & \\ \gamma_1 = 0.2, & \gamma_2 = 0.1, & \alpha_1 = 0.01, & \alpha_2 = 0.1 \\ d_{11} = 0.5, & d_{12} = 0.1 & d_{13} = 0.1 & \\ d_{22} = 0.3, & d_{33} = 0.1. & & \end{array} \tag{30}$$

Example 6 (Superinfection model)**.**

$$\begin{array}{cccc} \mu = 0.005 & r = 0.1 & A = 0.1 & K = 1 \\ \beta_1 = 0.3, & \beta_2 = 0.2, & \sigma = 0.3 & \\ \gamma_1 = 0.2, & \gamma_2 = 0.05, & \alpha_1 = 0.01, & \alpha_2 = 0.02 \\ d_{11} = 0.8, & d_{12} = -0.05 & d_{13} = -0.07 & \\ d_{22} = 0.03, & d_{33} = 0.5. & & \end{array} \tag{31}$$

Example 7. (Co-infection model)

$$\begin{array}{cccc} \mu = 0.005, & r = 0.1, & A = 0.1, & K = 1, \\ \beta_1 = 0.5, & \beta_2 = 0.4, & & \\ \beta_{10} = 0.4, & \beta_{02} = 0.3, & \beta_{12} = 0.15, & \\ \gamma_1 = 0.2, & \gamma_2 = 0.1, & & \\ \alpha_1 = 0.05, & \alpha_2 = 0.2, & \alpha_{12} = 0.15, & \\ d_{11} = 0.5, & d_{12} = 0.1, & d_{13} = 0.1, & \\ d_{22} = 0.2, & d_{33} = 0.3. & & \end{array} \tag{32}$$

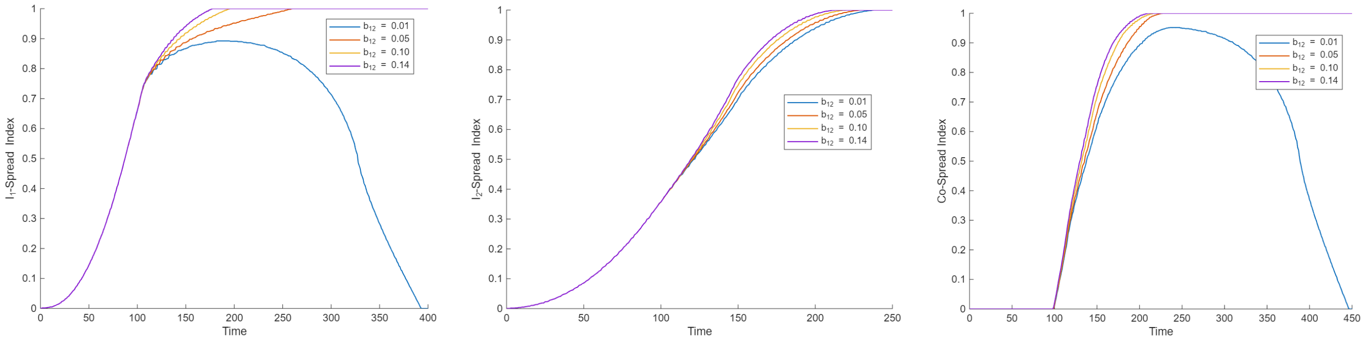

(a)

(b)

(c)

FIG. 21: I_1-spread index (left), I_2-spread index (center), and C-spread index (right) for four different values of β_{12}. Based on Example 4.

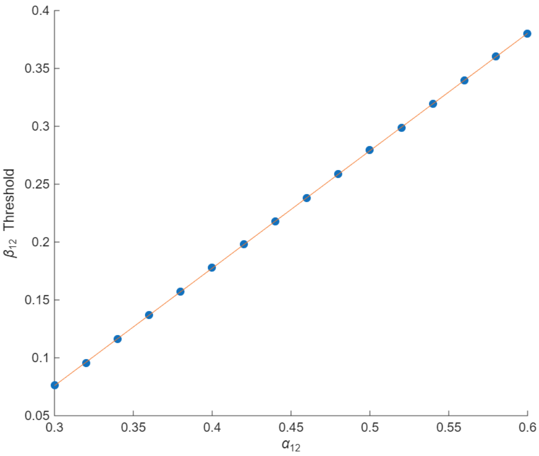

FIG. 22: β_{12}-threshold for varying α_{12} values. Fitted curve: $y = ax + b$, where $a = 1.0148$ and $b = -0.2285$.

Example 8. (Co-infection model)

$$\begin{array}{llll} \mu = 0.005, & r = 0.1, & A = 0.1, & K = 1, \\ \beta_1 = 0.7, & \beta_2 = 0.4, & & \\ \beta_{10} = 0.2, & \beta_{02} = 0.05, & \beta_{12} = 0.15, & \\ \gamma_1 = 0.2, & \gamma_2 = 0.1, & & \\ \alpha_1 = 0.16, & \alpha_2 = 0.05, & \alpha_{12} = 0.15, & \\ d_{11} = 0.8, & d_{12} = 0.05, & d_{13} = 0.05, & \\ d_{22} = 0.4, & d_{33} = 0.1. & & \end{array} \tag{33}$$

We first analyze infection diffusion for different network topology and layerwise average degrees in superinfection dynamics. We saw for the examples in Section VI that it may be optimal for the layerwise average degrees to vary. In this context, we expect something similar to occur. In particular, a lower average degree for the layer with J densities than the other two layers may be the most beneficial in slowing the spread of J so that it cannot dominate as much. We use Table II to verify this. The first subtable compares different combinations of degrees and the I_1-peak value, I_1 peak time, and I_2 saturation time that occur.

We start by focusing specifically on lattice networks because they are deterministic. We note that because pathogen 2 has a larger removal rate, we want to maximize the time that the $J-$spread index reaches 1 to lessen the number of deaths. From all of the subtables in Table II, we observe the following:

- We find that in all the subtables in Table II, the degree combinations that give the highest I_2 saturation times are LA24-LA12-LA4, LA12-LA4-LA4, LA12-LA12-LA4, and LA4-LA4-LA4. Thus, in superinfection dynamics, it is most paramount that the average degree of the J-density layer of the multiplex network are low.

- The average degree of the susceptible density layer has no significant impact on the I_1-peak value, I_1-peak time, and I_2-saturation time. For example, the LA24-LA12-LA4 produces a I_1 peak value of 1 but a I_2 saturation time of 184. Meanwhile, the LA12-LA12-LA4 also has the same I_1-peak and I_2 saturation values.

- Recent research has found that diffusion generally occurs faster in BA networks than WS networks [51, 52]. As a result, we expect that in BA networks, the number of instances of superinfection will grow earlier and faster, leading to smaller peaks in the I_1-spread index and a longer time for the I_2-spread index to reach 1. We verify this is true in Tables II, where the time that the I_2-spread index reaches 1 is consistently lower for BA networks than WS networks. Moreover, degree variations have a smaller impact on the values on the spread indexes over time for both infections. The BA network topology may also explain why outbreaks often occur during holidays and policies become less effective.

Moving to co-infection dynamics, we similarly expect that it is most beneficial for the graph corresponding to

Layerwise Degree Variations, using Examples 3, 5, 6 and Lattice Networks											
Network Type			**Example 3**			**Example 5**			**Example 6**		
S layer	I layer	J layer	I_1-peak value	I_1-peak time	I_2-sat. time	I_1-peak value	I_1-peak time	I_2-sat. time	I_1-peak value	I_1-peak time	I_2-sat. time
LA24	LA24	LA24	1	28	43	0.0006	0	38	0.0006	0	48
LA24	LA4	LA12	0.5056	71	74	0.0881	62	66	0.1581	84	60
LA24	LA12	LA4	1	49	184	0.6756	84	158	0.7963	99	128
LA12	LA12	LA12	0.9719	54	75	0.0969	60	66	0.3844	80	60
LA12	LA4	LA12	0.5056	71	74	0.0881	62	66	0.1581	84	60
LA12	LA4	LA4	0.8581	88	183	0.3444	111	158	0.3525	116	128
LA12	LA12	LA4	1	49	184	0.6756	84	158	0.7963	100	128
LA4	LA4	LA4	0.8581	88	183	0.3444	111	158	0.3525	116	128

Layerwise Degree Variations, using Example 3							
Average Degrees			**WS**			**BA**	
S layer	I layer	J layer	I_1-peak value	I_1-peak time	I_2-sat. time	I_1-sat. time	I_2-sat. time
24	24	24	1	21	25.01	21	24
24	4	12	0.9458	45.573	29.649	21	24
24	12	4	1	22.061	72.345	21	29.341
12	12	12	1	22.049	29.622	21	24
12	4	12	0.95034	45.721	29.555	21	24
12	4	4	0.99901	46.391	71.883	21.912	29.358
12	12	4	1	22.059	72.611	21	29.321
4	4	4	0.99874	46.353	72.434	21.913	29.348

Layerwise Degree Variations, using Example 5							
Average Degrees			**WS**			**BA**	
S layer	I layer	J layer	I_1-peak value	I_1-peak time	I_2-sat. time	I_1-peak value	I_2-sat. time
24	24	24	0.0006	0	21.041	0.000625	20
24	4	12	0.00063062	0.019	25.637	0.000625	20
24	12	4	0.000625	0	63.19	0.000625	25.464
12	12	12	0.000625	0	25.591	0.000625	20
12	4	12	0.00063062	0.02	25.644	0.000625	20
12	4	4	0.0013719	6.899	63.026	0.000625	25.494
12	12	4	0.000625	0	63.265	0.000625	25.482
4	4	4	0.0014444	6.631	62.924	0.000625	25.495

Layerwise Degree Variations, using Example 6							
Average Degrees			**WS**			**BA**	
S layer	I layer	J layer	I_1-peak value	I_1-peak time	I_2-peak time	I_1-peak value	I_2-sat. time
24	24	24	0.000625	0	47	0.0006	47
24	4	12	0.17353	77.012	47	0.0006	47
24	12	4	0.43153	78.423	64.423	0.0006	47
12	12	12	0.000625	0	47	0.0006	47
12	4	12	0.17657	77.039	47	0.0006	47
12	4	4	0.21016	79.89	64.475	0.0006	47
12	12	4	0.43003	77.688	64.422	0.0006	47
4	4	4	0.20097	79.75	64.365	0.0006	47

TABLE II: Variation of layerwise degrees with superinfection dynamics, each an average of 1000 trials.

the more dominant pathogen to have a lower average degree to slow the spread of that pathogen across the network. Table III incorporates the co-infection model in Equation 4 and the parameters from Example 4, 7, and 8. Here, we analyze each of them separately, as follows:

- **Example 4**. This parameter configuration satisfies $\alpha_{12} > \alpha_2 > \alpha_1$. Thus, it is most beneficial to limit the infections of pathogen 2, including co-infections. Overall, the combinations that produce the largest saturation time for I_2 and I_{12} are the LA12-LA4-LA4 and LA4-LA4-LA4. Moreover, for the LA24-LA4-LA12 and LA12-LA4-LA12, there is also a large saturation time for I_1.

Layerwise Degree Variations, using Examples 4, 7, 8 and Lattice Networks											
Network Type			**Example 4**			**Example 7**			**Example 8**		
S **layer**	I **layer**	J **layer**	I_1**-sat. time**	I_2**-sat. time**	C**-sat. time**	I_1**-sat. time**	I_2**-sat. time**	C**-sat. time**	I_1**-sat. time**	I_2**-sat. time**	C**-sat. time**
LA24	LA24	LA24	53	50	56	34	61	55	22	58	52
LA24	LA4	LA12	586	89	353	132	81	133	103	95	97
LA24	LA12	LA4	73	234	232	55	155	152	36	301	292
LA12	LA12	LA12	84	90	89	55	78	73	37	108	101
LA12	LA4	LA12	586	89	353	132	81	133	103	95	97
LA12	LA4	LA4	260	229	227	132	161	157	93	279	270
LA12	LA12	LA4	73	234	232	55	155	152	36	301	292
LA4	LA4	LA4	260	229	227	132	161	157	93	279	270

Layerwise Degree Variations, using Example 4								
Average Degrees			**WS**			**BA**		
S **layer**	I **layer**	J **layer**	I_1**-sat. time**	I_2**-sat. time**	C**-sat. time**	I_1**-sat. time**	I_2**-sat. time**	C**-sat. time**
24	24	24	42	30.997	49	42	30	49
24	4	12	206.54	35.534	109.15	42	30	49
24	12	4	47.186	86.964	87.678	43.798	30.154	50.412
12	12	12	44.741	35.522	50.677	42	30	49
12	4	12	205.06	35.519	108.87	42	30	49
12	4	4	79.151	85.998	88.342	44.495	35.139	50.394
12	12	4	47.269	87.004	87.816	43.823	35.156	50.462
4	4	4	80.926	85.362	88.37	44.548	35.12	50.396

Layerwise Degree Variations, using Example 7								
Average Degrees			**WS**			**BA**		
S **layer**	I **layer**	J **layer**	I_1**-sat. time**	I_2**-sat. time**	C**-sat. time**	I_1**-sat. time**	I_2**-sat. time**	C**-sat. time**
24	24	24	24	59	53	24	59	53
24	4	12	55.093	62.9	65.06	25	59	53
24	12	4	26.305	80.404	75.829	24	59	53
12	12	12	26.285	59	53.001	24	59	53
12	4	12	55.406	62.943	65.275	25	59	53
12	4	4	54.962	83.433	79.132	25	59	53
12	12	4	26.274	80.755	76.213	24	59	53
4	4	4	55.104	83.323	79.063	25	59	53

Layerwise Degree Variations, using Example 8								
Average Degrees			**WS**			**BA**		
S **layer**	I **layer**	J **layer**	I_1**-sat. time**	I_2**-sat. time**	C**-sat. time**	I_1**-sat. time**	I_2**-sat. time**	C**-sat. time**
24	24	24	18	26.059	29	18	25	29
24	4	12	35.974	33.44	38.772	18	25	29
24	12	4	18.599	121.13	111.84	18.676	34.168	32.378
12	12	12	18.536	34.862	32.733	18	25	29
12	4	12	36.073	33.423	38.907	18	25	29
12	4	4	35.407	116.22	106.95	18.915	34.313	32.459
12	12	4	18.602	121.28	111.97	18.668	34.155	32.389
4	4	4	35.654	116.21	106.86	18.923	34.227	32.409

TABLE III: Variation of layerwise degrees with coinfection dynamics, each an average of 1000 trials.

- **Example 7**. This parameter configuration satisfies $\alpha_2 > \alpha_{12} > \alpha_1$. Again, it is most beneficial to limit the infections of pathogen 2, including co-infections. In this case, the multiplex network combinations LA24-LA12-LA4, LA12-LA4-LA4, LA12-LA12-LA4, and LA4-LA4-LA4. Out of these, the combinations LA12-LA4-LA4 and LA4-LA4-LA4 produce the highest I_1-saturation times in addition to the high I_2 and and C-saturation time, and are thus most beneficial.

- **Example 8**. This parameter configuration satisfies $\alpha_1 > \alpha_{12} > \alpha_2$, where α_1 and α_{12} are only 0.01 apart. Thus, it may be most beneficial to limit the infections of pathogen 1, including co-infections. It is the most beneficial to maximize the saturation times for pathogen 1 and co-infections. Thus, the most beneficial layer combinations are LA12-LA4-LA4 and LA4-LA4-LA4.

As a result, to minimize the spread of both infections, it is most important to reduce the movement of individuals infected by either, and limiting the movement of susceptible individuals is less important.

In human metapopulations, migration patterns can be best described with the BA networks topologies. A key feature of scale-free networks such as BA networks is large hubs that dominate the network. This accurately reflects how during holiday season, major cities serve as large tourism hubs, as [53] shows is true for Chinese tourism on the May Day holiday.

During other seasons, human metapopulations are better represented with small-world networks such as the WS network. The WS network has a high clustering coefficient, representing how at work and local events, humans form many close social circles. Small-world networks are also characterized by short average path lengths, which represent how communities in human metapopulations are highly interconnected [21, 54].

Studies have shown that infections often spike during holidays [55, 56]. From the results discussed above, we observe for both superinfection and co-infection dynamics that BA network topologies allow both pathogens to spread more quickly throughout the network. As a result, we believe that network topology may be a reason for infection spikes during holiday seasons.

VIII. COMPARISON WITH REAL-WORLD INFECTIONS

In this section, we explore some of the similarities between our co-infection simulations and real-world data. First, we present two observations from our simulations, which are illustrated with Example 9. Then, we show that some of these phenomena can be found in real-world data.

We conduct simulations with the co-infection model in Equation (4) and the parameters in Example 9.

Example 9. (Co-infection model)

$$\begin{array}{llll}
\mu = 0.005, & r = 0.1, & A = 0.1, & K = 1, \\
\beta_1 = 0.4, & \beta_2 = 0.3, & & \\
\beta_{10} = 0.1, & \beta_{02} = 0.3, & \beta_{12} = 0.05, & \\
\gamma_1 = 0.1, & \gamma_2 = 0.05, & & \\
\alpha_1 = 0.01, & \alpha_2 = 0.02, & \alpha_{12} = 0.05, & \\
d_{11} = 0.3, & d_{12} = 0.001, & d_{13} = 0.001, & \\
d_{22} = 0.03, & d_{33} = 0.01. & &
\end{array} \tag{34}$$

Note that these figures show the density on each layer as a function of the node index. This leads us to some examples, shown in Figure 23. We have the following observations:

- It is a general pattern that oftentimes, the peaks of one infection and a valley of the other infection occur at the same location. We see this occur for different types of initializations, including when both initializations are far from each other and when they are close.

- The severity of both infections tend to be higher in locations that have a greater density of co-infections, and co-infection distributions tend to mirror the density distribution of one pathogen more than the other. This can be seen in Figure 23(a), co-infection distributions typically follow pathogen 1 infection distributions, but follows pathogen 2 infection distributions at some locations. In Figure 23(b), co-infection distributions typically follow pathogen 2 infection distributions, but follow pathogen 1 infection distributions at some locations. In Figure 23(c), co-infection distributions follow pathogen 2 infections from nodes 1 to 40, and pathogen 1 infections otherwise. Figure 23(d) is more of an anomaly because co-infection distributions tend to follow the spatial distribution of pathogen 1 infections throughout the entire network at $t = 9$. We see both through our simulations and real-world studies that in many cases, the co-infection trends tend to mirror those of the more severe pathogen.

Our second observation aligns with the conclusions in [57]. They investigate co-infections of different strains of the pathogen *Podosphaera plantaginis* in *Plantago lanceolata* gardens and find that overall infection severity is higher in local populations where co-infection rates are high. In our simulations, we also observe examples of this. Since the blue curve represents both pathogen 2 and co-infections, we see that in many cases when the co-infection curve peaks in Figure 23, this coincides with the a peak in the density of pathogen 2 infection densities, which include co-infections.

We also analyze the validity of both observations in the context of the co-circulation of COVID-19 and tuberculosis. The city of Recife, Brazil, can be broken down into 94 neighborhoods. Silva *et al.* examined the incidences of COVID-19, tuberculosis, and co-infections in this region in 2020 [58]. We assume that the incidences of COVID-19 and tuberculosis include co-infections. Figures 2-4 in [58] categorize the incidences in four categories for each type of infection. We record each region with "1", "2", "3", or "4", based on the category. We denote "1" to represent the category with the lowest incidences and "4" to represent the category with the highest incidences, and call these the i-th COVID, tuberculosis, and coinfection category numbers for region i. We see that for more than 35% of the regions, the absolute difference between the COVID and tuberculosis category numbers are greater than 2. Moreover, around 7% of the regions have an exact absolute difference of 3 between the COVID and tuberculosis category numbers, showing that peak and valleys can occur in the same region at the same time for different infections. On the other hand, we note that

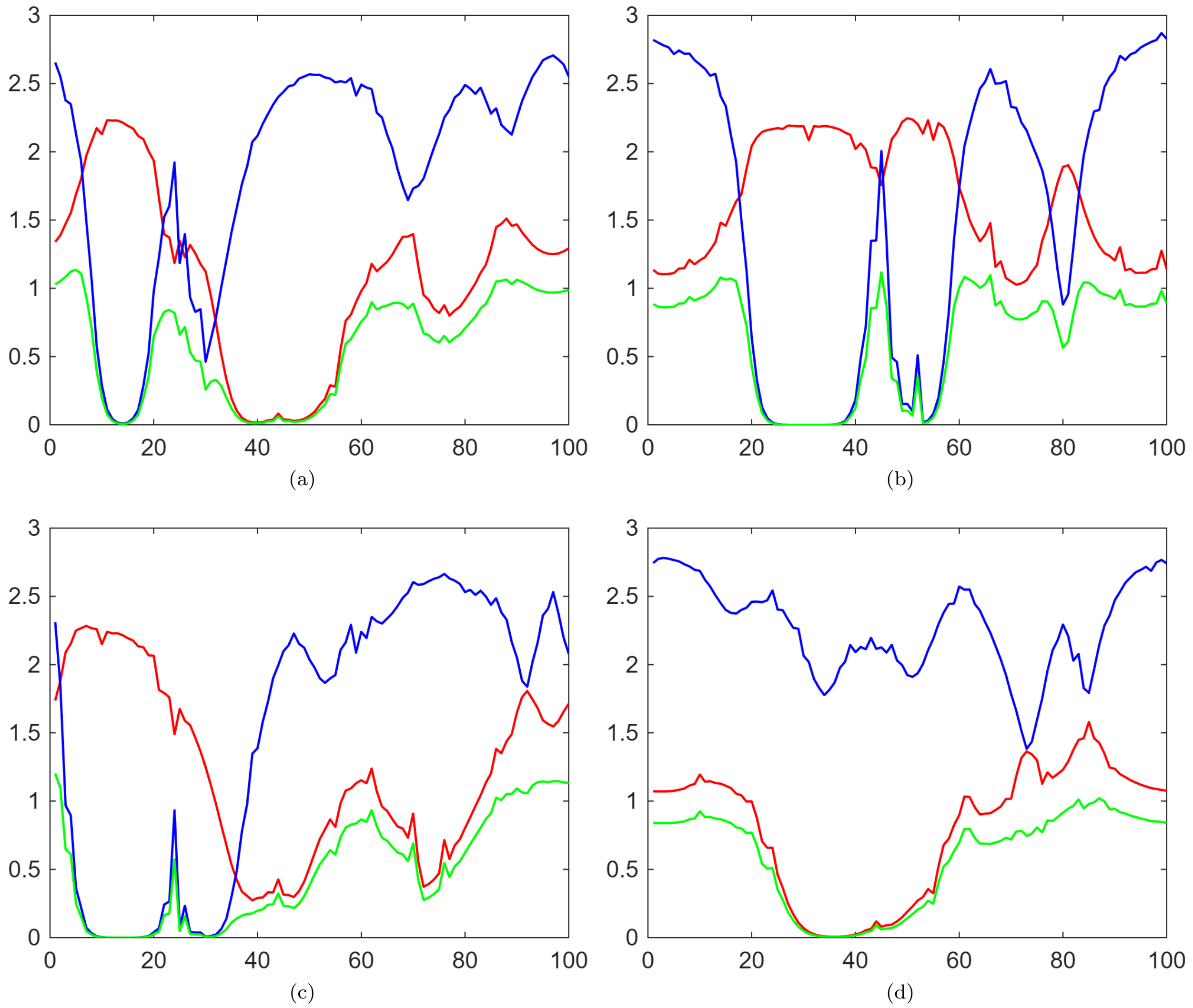

(a)

(b)

(c)

(d)

FIG. 23: At $t = 9$ with different infection initializations on WS (top row) and BA (bottom row) networks with 100 nodes. Red represents combined pathogen 1 and co-infection densities, blue represents combined pathogen 2 and co-infection densities, and green represents co-infection densities only.

around 87 percent of the time, the absolute differences between the tuberculosis and coinfection categories take on the values 0 or 1, showing that the spatial trends of coinfections closely resemble that of tuberculosis in this scenario. It is also worth noting that tuberculosis is generally considered to be the more severe disease.

We also look at Wu *et al.*'s analysis of tuberculosis and HIV co-infections from 2011-2019 in Jiangsu province [59]. We see that from 2011-2014 in particular, the northern side of Jiangsu province is filled with tuberculosis infection hotspots but is almost entirely an HIV cold spot. Moreover, many areas in the south are HIV hotspots are tuberculosis cold spots in the same years. Finally, we see that spatial co-infection distributions closely follow that of HIV infections, where the north is almost entirely a coldspot but there are some hotspots in the south, supporting our two simulation-based observations.

IX. APPLICATIONS

MBRD offers a framework upon which reaction-diffusion models can be created for other applications. In the following, we discuss potential applications of our framework.

- **Information propagation:** The super-infection model proposed in this paper can be used to analyze the spread of conflicting or related rumors in the same network of societies. In applications of the co-infection model to social networks, individuals may be thought of as "co-infected" if they change their mind frequently and therefore spread both rumors.

- **Malware propagation:** The models in this paper can be modified to study computer viruses on networks. First, it is important to understand the dynamics between viruses and anti-viruses.

Previous compartmental models have represented computers as susceptible, infected, or protected nodes [60]. This could be extended into reaction-diffusion equations on a three-multiplex network, where the three layers represent the three states of computers, using the framework in this paper. Superinfection-like phenomena can occur when one particular malware is particularly dominant. Second, there is evidence that computer viruses, such as Vobfus and Beebone [61], can infect a host computer at the same time and even support one another's survival. These dynamics can be analyzed with co-infection models similar to the one presented in this paper.

- **Urban planning:** Reaction-diffusion models on networks can describe how traffic congestion propagates from region to region, including how congestion in a city affects that of nearby suburbs or how freight transportation or school buses impact congestion at different times of the day. Models such as [62] can be modified to incorporate multiple transportation layers with road networks, commuter rail networks, or metro systems.

- **Election forecasting:** Compartmental epidemic models have been used to predict the 2012 and 2016 presidential elections [63]. These models can be extended to reaction-diffusion equations on networks to analyze the spatial dynamics between voting intentions of different smaller regions in the USA and other countries. An individual may be thought of as "superinfected" if they switch ideologies or are leaning towards one party but end up voting for another similar party that is more likely to win. Additionally, a voter can be thought of as "co-infected" if they are moderate or believe in different aspects of two or more ideologies and are unsure of which of those parties they will vote for.

X. FINAL REMARKS

Over the past years, we have seen a rise in the use of reaction-diffusion dynamics to model not only epidemic spread, but also for rumor propagation and predator-prey dynamics [21, 64, 65]. In this paper, we have introduced two new deterministic frameworks: the **Multiplex Bi-Virus Reaction-Diffusion models (MBRD)**. These include the **MBRD-SI** model for superinfection and the **MBRD-CI** model for co-infection, both formulated on multiplex metapopulation networks.

Prior research has utilized stochastic processes to model superinfection and co-infection dynamics [9, 66]. However, by integrating diffusion into our deterministic models, we capture an important characteristic of infection spread while offering computational simplicity. This makes the MBRD class of models well-suited for predicting epidemic"waves" and large-scale pattern formation.

Our MBRD-CI model, for example, could provide more accurate predictions of infections during the COVID-19 pandemic, where co-infection with influenza reached rates as high as 48% [67]. Indeed, it can be applied to pairwise co-infections of influenza, COVID-19, and Respiratory Syncytial Virus (RSV), assuming that immunity for COVID-19 is short-lived, or co-infections of gonorrhea and chlamydia [68]. On the other hand, the MBRD-SI model is well-suited for applications such as modeling HIV superinfection [69], where recovery does not occur and $\gamma_1 = \gamma_2 = 0$.

To our knowledge, this is the first work to establish superinfection and co-infection reaction-diffusion epidemic models on multiplex networks, as well as provide both theoretical and simulation-based analyses. Our work also involve deriving conditions for pattern formation involving three or four morphogens, which had not previously been analyzed in a network setting. Moreover, because spatial-temporal interactions between two pathogens have not been thoroughly analyzed in prior research, we also provide a simulation-based approach of analyzing both models to understand the spatial spread of both infections over time.

Summary of our results. We have the following observations:

- **Source separation.** We analyze how the initialization locations of both infections impact the dynamics across networks. When one infection is initialized at a lattice's center, a small source separation produces rapid overlap of infection fronts and faster saturation of co-infections across the network. Additionally, delayed interaction between spreading fronts and slower emergence of co-infected clusters occur for large source separations in the same configurations.

- **Migration** When migration rates are high, infection waves reach overlap earlier, and increased mixing leads to stronger co-infection presence across networks. On the other hand, low migration rate promotes lower propagation and weaker overlap, and pathogens remain localized longer.

- **Pathogen strength.** The stronger pathogen, which is typically accompanied by higher β or lower α values, tends to dominates in overlap regions and suppresses the weaker pathogen.

- **Multiplex network average degrees.** Variations in layerwise average degrees prevent pattern formation and increases in average degrees overall allow for larger clusters during pattern formation. Moreover, we find that reducing the average degrees of both the infection layers of the multiplex network is important for slowing the spread of both pathogens. Thus, we show that mitigation efforts should focus on limiting the movement of infectious individuals, with less priority on limiting the movement of susceptible individuals.

- **Network topology.** From comparing saturation times for different types of networks, we find that infections spread slower and are less severe in

Watts-Strogatz (WS) network topologies in comparison to Barabasi-Albert topologies (BA). Because BA topologies. Thus, network topology may provide a possible explanation for why outbreaks often occur during holiday seasons.

We have illustrated in this work that early containment of both types of infections is crucial to slowing the reach of these pathogens. Many previously implemented containment methods align with our findings. For example, quarantining of infection individuals was implemented during the COVID-19 pandemic [70] and the 2002-2004 SARS outbreak [71]. Moreover, border control policies for infected people prevent migration between regions, which correspond to reducing edges in our networks [72]. According to our findings, this is beneficial not only for the respective countries or regions, but also for the entire metapopulation.

Future Research Directions. This paper provides a foundation for which many extensions can be made. Future research building on the models introduced here could incorporate the following:

- Extending the present model to a system with 3, or in general n-pathogens, would be useful for modeling the interactions between COVID-19, influenza, and Respiratory Syncytial Virus (RSV) around the world between 2020 and 2023, among other scenarios.

- In many cases, human movement between two communities may be particularly large or small, or may only be one-directional. Accounting for these differences through weighted and directed networks may produce more accurate models for predicting infectious spread.

- The current SIS model cannot be directly applied to vector-borne diseases. A vector-borne adaptation of the co-infection model in Equation 4 can be used to investigate malaria and helminth co-infections [73], Zika and dengue co-infections [74], and COVID-19 and dengue co-infections [75]. Vector-borne adaptations of the superinfection model proposed in Equation 3 can be used to model different strains of dengue viruses [76], among others.

- The spread of infections is often influenced by environmental factors, such as temperature, humidity, and air quality [77]. In the future, the impact of these conditions on infection spread can be investigated and point-source infections can be investigated with stochastic noise factored in.

- The impact of various vaccination strategies and other specific mitigation strategies can be further investigated through simulations, or through formulating our model into an optimal control problem, similar to how [78] analyzes COVID-19 spread.

Acknowledgments.
I am grateful to my mentor Dr. Laura Schaposnik for her guidance and feedback throughout this process. I also thank the MIT PRIMES-USA program for their support and the opportunity to conduct this research.

References

[1] Alyssa Yu and Laura P. Schaposnik. Spatial superinfection and co-infection dynamics in networks. *arXiv preprint arXiv:2508.15740*, 2025.

[2] Maria Kiskowski and Gerardo Chowell. Modeling household and community transmission of ebola virus disease: epidemic growth, spatial dynamics and insights for epidemic control. *Virulence*, 7(2):163–173, 2016.

[3] JC Koella and Rustom Antia. Epidemiological models for the spread of anti-malarial resistance. *Malaria Journal*, 2:1–11, 2003.

[4] Editorial. How epidemiology has shaped the covid pandemic. *Nature*, 589(7843):491–492, 2021.

[5] Nina B Masters. Real-time use of a dynamic model to measure the impact of public health interventions on measles outbreak size and duration - chicago, illinois, 2024. *MMWR. Morbidity and Mortality Weekly Report*, 73, 2024.

[6] Georgios Pappas, Ismene J Kiriaze, and Matthew E Falagas. Insights into infectious disease in the era of hippocrates. *International journal of infectious diseases*, 12(4):347–350, 2008.

[7] Klaus Dietz and JAP Heesterbeek. Daniel bernoulli's epidemiological model revisited. *Mathematical biosciences*, 180(1-2):1–21, 2002.

[8] William Ogilvy Kermack and Anderson G McKendrick. A contribution to the mathematical theory of epidemics. *Proceedings of the royal society of london. Series A, Containing papers of a mathematical and physical character*, 115(772):700–721, 1927.

[9] Sebin Gracy, Philip E Paré, Ji Liu, Henrik Sandberg, Carolyn L Beck, Karl Henrik Johansson, and Tamer Başar. Modeling and analysis of a coupled sis bi-virus model. *Automatica*, 171:111937, 2025.

[10] G Ch Sirakoulis, Ioannis Karafyllidis, and Adonios Thanailakis. A cellular automaton model for the effects of population movement and vaccination on epidemic propagation. *Ecological Modelling*, 133(3):209–223, 2000.

[11] Alison Gray, David Greenhalgh, Liangjian Hu, Xuerong Mao, and Jiafeng Pan. A stochastic differential equation sis epidemic model. *SIAM Journal on Applied Mathematics*, 71(3):876–902, 2011.

[12] Ioanna A Mitrofani and Vasilis P Koutras. A branching process model for the novel coronavirus (covid-19) spread in greece. *Int. J. Model. Optim*, 11(3), 2021.

[13] Yuyuan Luo and Laura P Schaposnik. Minimal percolating sets for mutating infectious diseases. *Physical Review Research*, 2(2):023001, 2020.

[14] Vishaal Ram and Laura P Schaposnik. A modified age-structured sir model for covid-19 type viruses. *Scientific reports*, 11(1):15194, 2021.

[15] Kazeem Babatunde Akande, Samuel Tosin Akinyemi, Nneka O Iheonu, Alogla Monday Audu, Folashade Mistura Jimoh, Atede Anne Ojoma, Victoria Iyabode Okeowo, Abdulrahaman Lawal Suleiman, and Kayode Oshinubi. A risk-structured model for the transmission dynamics of anthrax disease. *Mathematics*, 12(7):1014, 2024.

[16] Herbert W Hethcote. Qualitative analyses of communicable disease models. *Mathematical biosciences*, 28(3-4):335–356, 1976.

[17] Chia-Hsien Lin and Tzai-Hung Wen. How spatial epidemiology helps understand infectious human disease transmission. *Tropical Medicine and Infectious Disease*, 7(8):164, 2022.

[18] Xing Gao, Gang Li, Jiaobei Wang, and Tingting Xu. Spatiotemporal evolution, pattern of diffusion, and influencing factors of the covid-19 epidemic in hainan province, china. *Journal of Medical Virology*, 94(4):1581–1591, 2022.

[19] Vaishnavi Thakar. Unfolding events in space and time: Geospatial insights into covid-19 diffusion in washington state during the initial stage of the outbreak. *ISPRS International Journal of Geo-Information*, 9(6):382, 2020.

[20] Moran Duan, Lili Chang, and Zhen Jin. Turing patterns of an si epidemic model with cross-diffusion on complex networks. *Physica A: statistical mechanics and its applications*, 533:122023, 2019.

[21] Bingrui Zhao and Jianwei Shen. Navigating epidemic spread through multiplex networks: Unveiling turing instability and cross-diffusion dynamics. *Physica A: Statistical Mechanics and its Applications*, 660:130312, 2025.

[22] Irina Kalabikhina and Alexander Panin. Spatial choreography of the coronavirus. 2020.

[23] Michael Emch, Mohammad Yunus, Veronica Escamilla, Caryl Feldacker, and Mohammad Ali. Local population and regional environmental drivers of cholera in bangladesh. *Environmental Health*, 9(1):2, 2010.

[24] Volker H Hackert, Wim van der Hoek, Nicole Dukers-Muijrers, Arnout de Bruin, Sascha Al Dahouk, Heinrich Neubauer, Cathrien A Bruggeman, and Christian JPA Hoebe. Q fever: single-point source outbreak with high attack rates and massive numbers of undetected infections across an entire region. *Clinical Infectious Diseases*, 55(12):1591–1599, 2012.

[25] Jack A Korlath, Michael T Osterholm, Lawrence A Judy, Jan C Forfang, and R Ashley Robinson. A point-source outbreak of campylobacteriosis associated with consumption of raw milk. *Journal of infectious diseases*, 152(3):592–596, 1985.

[26] Hans Meinhardt and Alfred Gierer. Pattern formation by local self-activation and lateral inhibition. *Bioessays*, 22(8):753–760, 2000.

[27] Vincent Castets, Etiennette Dulos, Jacques Boissonade, and Patrick De Kepper. Experimental evidence of a sustained standing turing-type nonequilibrium chemical pattern. *Physical review letters*, 64(24):2953, 1990.

[28] Benjamin M Alessio and Ankur Gupta. Diffusiophoresis-enhanced turing patterns. *Science Advances*, 9(45):eadj2457, 2023.

[29] Philip K Maini and Thomas E Woolley. The turing model for biological pattern formation. *The dynamics of biological systems*, pages 189–204, 2019.

[30] Hiroya Nakao and Alexander S Mikhailov. Turing patterns in network-organized activator–inhibitor systems. *Nature Physics*, 6(7):544–550, 2010.

[31] GF Webb. A reaction-diffusion model for a deterministic diffusive epidemic. *Journal of Mathematical Analysis and Applications*, 84(1):150–161, 1981.

[32] Zhenguo Bai, Rui Peng, and Xiao-Qiang Zhao. A reaction–diffusion malaria model with seasonality and incubation period. *Journal of mathematical biology*, 77:201–228, 2018.

[33] Laiquan Wang, Arshad Alam Khan, Saif Ullah, Nadeem

Haider, Salman A AlQahtani, and Abdul Baseer Saqib. A rigorous theoretical and numerical analysis of a nonlinear reaction-diffusion epidemic model pertaining dynamics of covid-19. *Scientific Reports*, 14(1):7902, 2024.

[34] Yangyang Shi and Hongyong Zhao. Analysis of a two-strain malaria transmission model with spatial heterogeneity and vector-bias. *Journal of Mathematical Biology*, 82:1–44, 2021.

[35] Fangzheng Lu, Yunbo Tu, and Xinzhu Meng. Application of a reaction–diffusion model with different incidence rates: Covid-19 strains evolution. *Nonlinear Dynamics*, 112(23):21533–21561, 2024.

[36] Martin A Nowak and Robert Mccredie May. Superinfection and the evolution of parasite virulence. *Proceedings of the Royal Society of London. Series B: Biological Sciences*, 255(1342):81–89, 1994.

[37] Marc Choisy and Jacobus C de Roode. Mixed infections and the evolution of virulence: effects of resource competition, parasite plasticity, and impaired host immunity. *The American Naturalist*, 175(5):E105–E118, 2010.

[38] Samuel Alizon. *Dynamics and evolution of infectious diseases.* PhD thesis, Université Montpellier 2, 2013.

[39] Daozhou Gao, Travis C Porco, and Shigui Ruan. Coinfection dynamics of two diseases in a single host population. *Journal of mathematical analysis and applications*, 442(1):171–188, 2016.

[40] Vit Piskovsky. Turing instabilities for three interacting species. *Applied Mathematics Letters*, 159:109269, 2025.

[41] Hans G Othmer and LE Scriven. Instability and dynamic pattern in cellular networks. *Journal of theoretical biology*, 32(3):507–537, 1971.

[42] Duncan J Watts and Steven H Strogatz. Collective dynamics of “small-world” networks. *nature*, 393(6684):440–442, 1998.

[43] Albert-László Barabási and Eric Bonabeau. Scale-free networks. *Scientific american*, 288(5):50–9, 2003.

[44] Jörn Davidsen, Holger Ebel, and Stefan Bornholdt. Emergence of a small world from local interactions: Modeling acquaintance networks. *Physical review letters*, 88(12):128701, 2002.

[45] Jon Kleinberg. The small-world phenomenon: An algorithmic perspective. In *Proceedings of the thirty-second annual ACM symposium on Theory of computing*, pages 163–170, 2000.

[46] Albert-László Barabási, Réka Albert, and Hawoong Jeong. Scale-free characteristics of random networks: the topology of the world-wide web. *Physica A: statistical mechanics and its applications*, 281(1-4):69–77, 2000.

[47] Mihaela Peres, Helian Xu, and Gang Wu. Community evolution in international migration top1 networks. *PloS one*, 11(2):e0148615, 2016.

[48] Moshe Levy. Scale-free human migration and the geography of social networks. *Physica A: Statistical Mechanics and its Applications*, 389(21):4913–4917, 2010.

[49] Purwanto Purwanto, Sugeng Utaya, Budi Handoyo, Syamsul Bachri, Ike Sari Astuti, Kresno Sastro Bangun Utomo, and Yulius Eka Aldianto. Spatiotemporal analysis of covid-19 spread with emerging hotspot analysis and space–time cube models in east java, indonesia. *ISPRS International Journal of Geo-Information*, 10(3):133, 2021.

[50] Jonas T Doumatè, Tahir B Issa, and Rachidi B Salako. Competition-exclusion and coexistence in a two-strain sis epidemic model in patchy environments. *arXiv preprint arXiv:2308.10348*, 2023.

[51] Linhe Zhu, Yue Li, Le He, and Shuling Shen. Pattern formation of network epidemic model and its application in oral medicine. *Computer Methods and Programs in Biomedicine*, 264:108688, 2025.

[52] Chunhua Ju, Yihao Jiang, Fuguang Bao, Bilin Zou, and Chonghuan Xu. Online rumor diffusion model based on variation and silence phenomenon in the context of covid-19. *Frontiers in Public Health*, 9:788475, 2022.

[53] Shanshan Wu, Lucang Wang, and Haiyang Liu. Study on tourism flow network patterns on may day holiday. *Sustainability*, 13(2):947, 2021.

[54] Marcel Salathé, Maria Kazandjieva, Jung Woo Lee, Philip Levis, Marcus W Feldman, and James H Jones. A high-resolution human contact network for infectious disease transmission. *Proceedings of the national academy of sciences*, 107(51):22020–22025, 2010.

[55] Björn Thor Arnarson. How a school holiday led to persistent covid-19 outbreaks in europe. *Scientific Reports*, 11(1):24390, 2021.

[56] Jiaying Qiao and Hiroshi Nishiura. Public holidays increased the transmission of covid-19 in japan, 2020-2021: a mathematical modelling study. *Epidemiology and Health*, 46:e2024025, 2024.

[57] Hanna Susi, Benoit Barrès, Pedro F Vale, and Anna-Liisa Laine. Co-infection alters population dynamics of infectious disease. *Nature communications*, 6(1):5975, 2015.

[58] Alene Bezerra Araújo Silva, Wayner Vieira de Souza, José Constantino Silveira Júnior, Juliana Silva de Santana, and Ricardo Arraes de Alencar Ximenes. Spatial analysis of tuberculosis, covid-19, and tuberculosis/covid-19 coinfection in recife, pe, brazil. *International Journal of Environmental Research and Public Health*, 22(4):545, 2025.

[59] Zhuchao Wu, Gengfeng Fu, Qin Wen, Zheyue Wang, Linen Shi, Beibei Qiu, and Jianming Wang. Spatiotemporally comparative analysis of hiv, pulmonary tuberculosis, hiv-pulmonary tuberculosis coinfection in jiangsu province, china. *Infection and Drug Resistance*, pages 4039–4052, 2023.

[60] JB Shukla, Gaurav Singh, Poonam Shukla, and Agraj Tripathi. Modeling and analysis of the effects of antivirus software on an infected computer network. *Applied Mathematics and Computation*, 227:11–18, 2014.

[61] Microsoft. Pair of pc viruses help each other survive, 2013.

[62] Leonardo Bellocchi and Nikolas Geroliminis. Unraveling reaction-diffusion-like dynamics in urban congestion propagation: Insights from a large-scale road network. *Scientific reports*, 10(1):4876, 2020.

[63] Alexandria Volkening, Daniel F Linder, Mason A Porter, and Grzegorz A Rempala. Forecasting elections using compartmental models of infection. *SIAM Review*, 62(4):837–865, 2020.

[64] Yong Ye, Jiaying Zhou, and Yi Zhao. Pattern formation in reaction-diffusion information propagation model on multiplex simplicial complexes. *Information Sciences*, 689:121445, 2025.

[65] Mingrui Song, Shupeng Gao, Chen Liu, Yue Bai, Lei Zhang, Beilong Xie, and Lili Chang. Cross-diffusion induced turing patterns on multiplex networks of a predator–prey model. *Chaos, Solitons & Fractals*, 168:113131, 2023.

[66] Qingchu Wu, Michael Small, and Huaxiang Liu. Superinfection behaviors on scale-free networks with competing strains. *Journal of nonlinear science*, 23(1):113–127, 2013.

[67] Cynthia Y Tang, Maria Boftsi, Lindsay Staudt, Jane A

McElroy, Tao Li, Sabrina Duong, Adrienne Ohler, Detlef Ritter, Richard Hammer, Jun Hang, et al. Sars-cov-2 and influenza co-infection: A cross-sectional study in central missouri during the 2021–2022 influenza season. *Virology*, 576:105–110, 2022.

[68] Jie Liang, Xiaoli Wang, Ying Lin, Ming He, Qian Sun, Xiang Li, Wenjing Zhang, Li Chang, Hui Guo, Rui Zeng, Zhen Liu, Lei Yang, and Su Hon. Mitigating co-circulation of seasonal influenza and covid-19 in the presence of vaccination: An age-specific co-epidemic model. *Frontiers in Cellular and Infection Microbiology*, 14:1347710, 2024.

[69] Andrew D Redd, Thomas C Quinn, and Aaron AR Tobian. Frequency and implications of hiv superinfection. *The Lancet infectious diseases*, 13(7):622–628, 2013.

[70] Zaibunnisa Memon, Sania Qureshi, and Bisharat Rasool Memon. Assessing the role of quarantine and isolation as control strategies for covid-19 outbreak: a case study. *Chaos, Solitons & Fractals*, 144:110655, 2021.

[71] Ying-Hen Hsieh, Chwan-Chuan King, Cathy WS Chen, Mei-Shang Ho, Sze-Bi Hsu, and Yi-Chun Wu. Impact of quarantine on the 2003 sars outbreak: a retrospective modeling study. *Journal of theoretical biology*, 244(4):729–736, 2007.

[72] Hiroshi Nishiura, Nick Wilson, and Michael G Baker. Quarantine for pandemic influenza control at the borders of small island nations. *BMC infectious diseases*, 9(1):27, 2009.

[73] Tabitha W Mwangi, JM Bethony, and Simon Brooker. Malaria and helminth interactions in humans: an epidemiological viewpoint. *Annals of Tropical Medicine & Parasitology*, 100(7):551–570, 2006.

[74] Ebenezer Bonyah, Muhammad Altaf Khan, Kazeem Oare Okosun, and JF Gómez-Aguilar. On the co-infection of dengue fever and zika virus. *Optimal Control Applications and Methods*, 40(3):394–421, 2019.

[75] Morgane Verduyn, Nathalie Allou, Virgile Gazaille, Michel Andre, Tannvir Desroche, Marie-Christine Jaffar, Nicolas Traversier, Cecile Levin, Marie Lagrange-Xelot, Marie-Pierre Moiton, and Stella Hoang. Co-infection of dengue and covid-19: A case report. *PLOS Neglected Tropical Diseases*, 14(8):e0008476, 2020.

[76] Adetayo Samuel Eegunjobi, Michael Chimezie Anyanwu, and SN Neossi-Nguetchue. Modelling the super-infection of two strains of dengue virus. *Journal of the Egyptian mathematical Society*, 31(1):1, 2023.

[77] Chacha M Issarow, Nicola Mulder, and Robin Wood. Environmental and social factors impacting on epidemic and endemic tuberculosis: a modelling analysis. *Royal Society open science*, 5(1):170726, 2018.

[78] Legesse Lemecha Obsu and Shiferaw Feyissa Balcha. Optimal control strategies for the transmission risk of covid-19. *Journal of biological dynamics*, 14(1):590–607, 2020.

Declaration of Academic Integrity

The participating team declares that the paper submitted is comprised of original research and results obtained under the guidance of the instructor. To the team's best knowledge, the paper does not contain research results, published or not, from a person who is not a team member, except for the content listed in the references and the acknowledgment. If there is any misinformation, we are willing to take all the related responsibilities.

Names of team members: Alyssa Yu

Signatures of team members:

Name of the instructor: Laura Schaposnik

Signature of the instructor:

Laura Schaposnik

Date: 8/24/2025